5

In Situ Measurement of the Inherent Optical Properties (IOPs) and Potential for Harmful Algal Bloom Detection and Coastal Ecosystem Observations

Collin S. Roesler and Emmanuel Boss

5.1 Introduction

Until recently, oceanographers and other aquatic scientists depended upon simple optical instruments, such as chlorophyll fluorometers and nephelometers or single-wavelength transmissometers, to estimate the distributions of phytoplankton and other suspended particles, respectively. During the last decade, technological advances and commensurate developments on optical modeling now make it possible to measure in situ and interpret the spectral inherent optical properties (IOPs) of the particulate and dissolved constituents of aquatic system. The capability for estimating biogeochemical properties from optical measurements, which, in combination with moored, profiling, and drifting platforms, has opened up new opportunities for studying ecosystem dynamics in general, and harmful algal blooms (HABs) specifically, on time and space scales that were never before possible (Chapter 3, Schofield et al., 2005). The limitations to this approach (i.e. IOP-based biogeochemical proxies) reside in the differences between the IOP theory (covered in Chapter 4, Morel, 2005) and the IOP measurement reality that results from the physical and environmental limitations of instrumentation (covered in this chapter), and finally with the assumptions associated with incorporating observations into models (covered in Chapter 7, Sosik, 2005).

The inherent optical properties of a medium describe the probability for light absorption and scattering, a and b, respectively, and their sum, the beam attenuation, c. When the medium is a complex mixture, its bulk IOPs can be expressed by the linear sum of the IOPs for each individual constituent:

$$a(\lambda) = \Sigma_{i=1}^{N} \; a_i(\lambda) \tag{1a}$$

$$b(\lambda) = \Sigma_{j=1}^{M} \; b_j(\lambda) \tag{1b}$$

where λ is wavelength, i and j indicate the individual constituents and N and M are the total number of absorbing and scattering constituents, respectively. In an aquatic medium, the bulk IOPs will be the sum of the IOPs for water itself and all of the solutes and particles contained in it. Because it is an impossible task to measure the IOPs of each individual constituent, they are

grouped into operational components based upon the spectral similarity of their IOPs or based upon analytic definitions.

Absorption is operationally separated into particulate and dissolved components where the separation is defined by the nominal pore size of a filter (typically 0.2 μm to 0.7 μm[1]). The dissolved fraction, while comprised of a very complex mixture of organic molecules, has an absorption spectrum with a relatively invariant spectral shape, exponentially decreasing from the ultraviolet to the red end of the spectrum (Bricaud et al., 1981; Roesler et al., 1989; Babin et al., 2003; Figure 5.1). The major variation is in the exponential slope coefficient, which responds to changes in composition and size distribution of the organic molecules (Carder et al., 1989; c.f. Twardowski et al., 2004). The absorption by particulate material (Figure 5.1) is further separated into phytoplankton and non-algal particles (NAP), the division of which is operationally based upon extractive techniques in which the total particulate matter is chemically depigmented and scanned, and the difference between the total particle absorption and the depigmented particle absorption is the *in vivo* absorption by phytoplankton pigments (Ducha and Kubin, 1976;

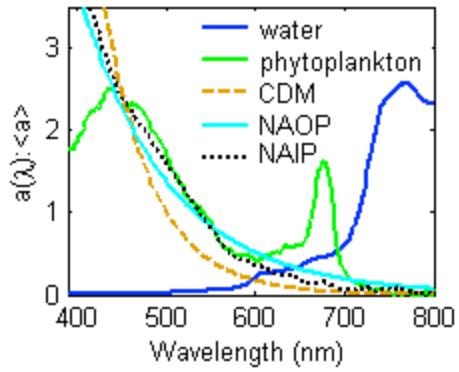

Figure 5.1. Characteristic absorption spectra for bulk seawater constituents normalized to the mean absorption: water (dark blue), phytoplankton (green), colored dissolved matter (dash orange), non-algal particulate organic matter (solid cyan), non-algal particulate inorganic matter (dotted black).

[1]The selection of a single pore size to separate the particulate and dissolved fractions has not been resolved by the community, in part because neither truly removes all the particles from the medium, although obviously the 0.2 μm pore size is closest. However, a 0.7 μm pore size is used when one wants to find the total absorption coefficient of a discrete sample analyzed spectrophotometrically: particles are concentrated on glass fiber filters (nominal pore size 0.7 μm) and dissolved samples obtained from the filtrate. Summing the two provides the total absorption. If, however, the 0.2 μm filtrate is used for the dissolved fraction, the total absorption is significantly underestimated by the 0.2 μm to 0.7 μm fraction which contains colloidal particles. In situ absorption measurements using the 0.2 μm filter are closer to the particulate/dissolved distinction but cannot hope to compare with discrete samples using the quantitative filter technique (which incorporates a 0.7-μm pore sized glass fiber filter) and its filtrate. Thus, when one wants to compare in situ absorption observations with discrete ones, it is recommended that glass fiber filters of nominal pore size 0.7 μm be used in both applications, with the understanding that the "dissolved" fraction contains large colloidal particles, which have their own dynamics separate from particulate and dissolved fractions (e.g. Simeon et al., 2003; Etheridge and Roesler, 2004).

Kishino et al., 1985; Roesler and Perry, 1995). The non-algal particulate matter is comprised of the non-pigmented portion of phytoplankton cells, bacteria and zooplankton, detrital material (which leads to the misnomer for this component as detrital absorption) and mineralic and biogenic inorganic particles. The grouping of these diverse constituents into a single component is in part due to the extractive method separating them from the algal pigments and in part due to the similarity in the absorption spectra, which also decays exponentially from blue to red, albeit with a different slope from the dissolved fraction (Iturriaga and Siegel, 1989; Roesler et al., 1989; Morel and Ahn, 1990; 1991). In regions with high mineralic particle concentrations, separating the NAP absorption into organic and inorganic components has proven difficult because they are spectrally similar in the visible range (Stramski et al., 2001; Babin and Stramski, 2002; 2005) and because chemical or combustive methods to remove the organic material (i.e. Werdell and Roesler, 2003; Etheridge and Roesler, 2004) may not result in additive absorption coefficients (i.e. may not obey eqn. 1a). For example, natural inorganic particles, which include both mineralic sediments and biogenic inorganic matter, are also subject to organic coating, causing them to resemble organic particles. Removing the organic coating, which is what was contributing to the in situ absorption, will result in the inorganic particle absorption, which was not contributing to the in situ absorption. Thus, unlike the extractive technique to separate phytoplankton and non-algal particle absorption, which is additive, the organic and inorganic separation is not additive and the resulting inorganic particle absorption may exceed the NAP absorption, may exhibit distinctive peaks associated with mineralic content (Babin and Stramski, 2002), or may be modified by the impacts of combustion (Babin and Stramski, 2005).

Particle scattering coefficients vary as a function of particle size and composition (the latter of which is manifested by the real and imaginary refractive indices[2]; Figure 5.2). For weakly absorbing particles, the scattering is a smoothly varying function of wavelength, the slope of which is related to the size distribution of the particles and the magnitude of which is a function of the concentration and the real index of refraction (itself a function of wavelength, e.g. Aas, 1996). For strongly absorbing particles such as phytoplankton, models predict that the

[2] Throughout this chapter, the indices of refraction are those relative to pure water. See Chapter 3 (Morel and Lewis, 2005).

scattering spectra exhibit distinct minima near the absorption peaks due to anomalous dispersion (van de

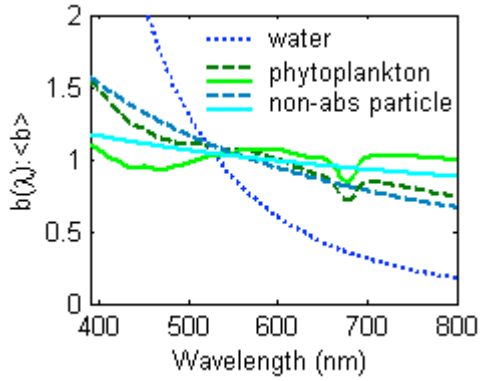

Figure 5.2. Characteristic scattering spectra for major constituents normalized to the mean scattering: water (dotted dark blue), large and small phytoplankton (solid green and dashed dark green, respectively), and large and small weakly absorbing particles (solid cyan and dashed blue, respectively.

Hulst, 1957; Morel and Bricaud, 1981; Zaneveld and Kitchen, 1995); such patterns are also observed in natural particle populations (Babin et al., 2002). By definition, the dissolved fraction would not contribute to scattering because it does not contain particles; however, the filtrate from even a 0.2-µm filter does contain submicron colloidal particles that do scatter light, as well as particles larger than the pore size, which pass through the filter due to both flexible pore boundaries and cell walls/membranes (e.g. Logan, 1993; Sosik et al., 2003). The angular dependence of scattering, described by the volume scattering function, also varies as a function of particle size and composition, as will be outlined in detail below.

To first order the component IOPs are a function of the component concentration:

$$a(\lambda) = a_w(\lambda) + C_\varphi\, a^*_\varphi(\lambda) + C_{CDM}\, a^*_{CDM}(\lambda) + C_{NAOP}\, a^*_{NAOP}(\lambda) + C_{NAIP}\, a^*_{NAIP}(\lambda) \quad (2a)$$

$$b(\lambda) = b_w(\lambda) + C_\varphi\, b^*_\varphi(\lambda) + C_{NAOP}\, b^*_{NAOP}(\lambda) + C_{NAIP}\, b^*_{NAIP}(\lambda) \quad (2b)$$

where C indicates concentration[3], a^* and b^* are the concentration-specific absorption and scattering coefficients[4], and the subscripts w and φ indicate water and phytoplankton, and CDM indicates chromophoric dissolved matter (operationally includes both organic and inorganic matter), and the non-algal particles are presented by both their organic and inorganic constituents

[3] The units on C will vary depending upon normalization of the optical property. For example, if a^*_φ is the chlorophyll-specific phytoplankton absorption coefficient ($m^2.mg^{-1}$), C, would be the chlorophyll concentration ($mg.m^{-3}$). Likewise if b^*_{NAIP} is the mass-specific inorganic particle scattering coefficient ($m^2.mg^{-1}$), C_{NAIP} would be the total inorganic particulate mass ($mg.m^{-3}$).

[4] The concentration-specific component absorption and scattering spectra are determined from either natural samples which have been separated as discussed above or generated in the laboratory from pure cultures (in the case of the phytoplankton component) or pure mineral suspensions (as in the case of NAIP).

(NAOP and NAIP, respectively). To second order, these component IOPs vary as a function biogeochemical composition. These variations are generally manifested as variations in the spectral shape of a^* and b^*, but may also impact the magnitude. For example, as the phytoplankton species composition and dominant size class change, the spectral shape of a_φ^* will vary in response to the changes in the in vivo composition and intracellular concentration of pigments (Bricaud et al., 1988; Sathyendranath et al., 1987; Sosik and Mitchell, 1991).

It is the dependence of the component IOPs, and hence the bulk IOPs, on the concentration, composition, and size distribution that make them ideal parameters to include in coastal observation systems for monitoring ecosystem dynamics and harmful algal blooms. The recent explosion in opto-electronic technology and the resulting emergence of a suite of in situ IOP sensors, which can be deployed on a range of platforms, has yielded the capability, for the first time, to measure biogeochemical indices on the same time and space scales as hydrographic and hydrodynamic properties, thereby permitting the relationships between environmental conditions and HAB events to be observed and quantified in real time. This capability lies at the heart of employing in situ IOP observations as an integral component of HAB detection. The key is to (1) measure the IOPs accurately, (2) optimize the IOP measurements with respect to biogeochemical variability, (3) quantify the IOP response to biogeochemical variations, and (4) deconvolve the IOPs into the desired biogeochemical parameters (e.g. generate optical proxies for biogeochemical parameters, Claustre et al., 2000). This chapter will address topics 1 and 2 in detail using examples from topic 3. Topic 4 will be the subject of Chapter 7 (Sosik, 2005).

5.2 IOP concepts and measurement theory

The IOPs are defined as those properties describing the probability of photon removal and photon redirection. As outlined in chapter 4 (Morel, 2005) these properties are the absorption, scattering and beam attenuation coefficients (a, b, and c, respectively), where

$$c = a + b, \tag{3}$$

and the volume scattering function (VSF; β). The VSF describes the angular distribution of scattering relative to the direction of light propagation, θ, and azimuthal angle φ. The scattering coefficient is the integration of β over all θ and φ (i.e. solid angles):

$$b = \int_0^{2\pi} \int_0^{\pi} \beta(\theta,\varphi) \sin\theta \, d\theta \, d\varphi \quad . \tag{4a}$$

In natural waters, where particles are assumed to be randomly oriented, azimuthal symmetry is assumed (i.e. scattering independent of φ) and the scattering coefficient is represented by:

$$b = 2\pi \int_0^{\pi} \beta(\theta) \sin\theta \, d\theta \, . \tag{4b}$$

The backscattering coefficient is the integral of β over the backward hemisphere, relative to the incident radiance (Figure 5.3):

$$b_b = 2\pi \int_{\pi/2}^{\pi} \beta(\theta) \sin\theta \, d\theta \, . \tag{5}$$

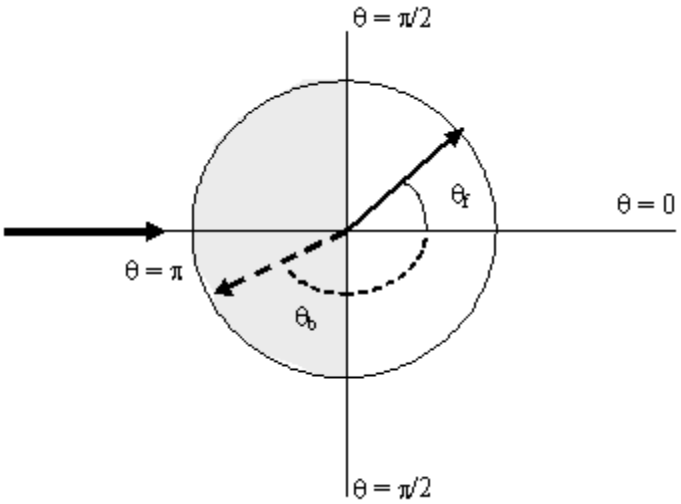

Figure 5.3. Diagram of the scattering angles, θ, where the bold arrow at left signifies the incident beam, forward scattering is indicated by the solid arrow and angle θ_f, and backscattering by the dashed arrow and angle θ_b. Forward scattering occurs in the forward white hemisphere ($\theta = 0$ to $\pi/2$) while backscattering occurs in the backward shaded hemisphere ($\theta = \pi/2$ to π) and azimuthal symmetry is assumed. In a bulk sense, the symmetry assumption holds in the ocean because, although particles are neither spherical nor homogeneous, they are randomly oriented.

The definitions of the IOPs with respect to measurement can be visualized by an infinitesimally thin layer (thickness Δr) of medium illuminated by a plane wave of monochromatic light incident perpendicular to the layer (Figure 5.4). The conservation of power indicates that the fate of the incident radiant flux, Φ_o, on this layer is either absorption, scattering or transmittance, where Φ_A, Φ_B, and Φ_T are the absorbed, scattered and transmitted radiant flux, and, by conservation of energy:

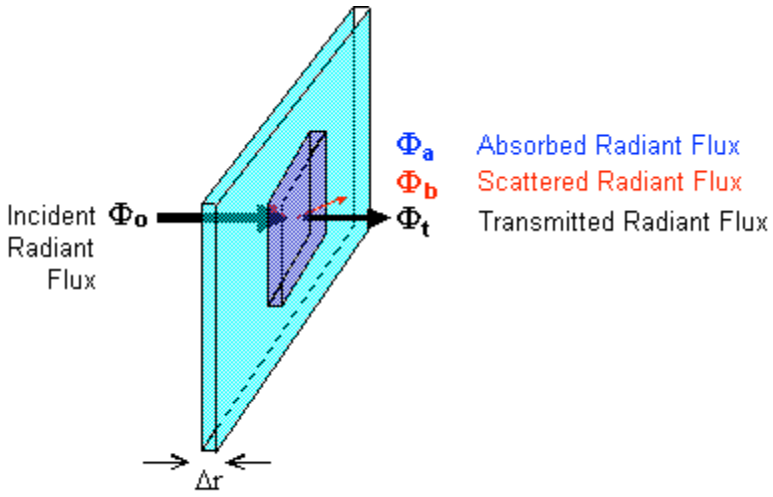

Figure 5.4. Conceptual diagram of radiant flux through an infinitesimal layer of thickness Δr. Energy is conserved such that the incident flux is either scattered by the layer (red), absorbed by material in the layer (blue), or transmitted through the layer unattenuated (black).

$$\Phi_o = \Phi_A + \Phi_B + \Phi_T \,. \tag{6}$$

The absorptance, scatterance and transmittance (A, B, and T, respectively) are defined as the fractions of incident power absorbed, scattered and transmitted, and are given by (e.g. Kirk, 1994):

$$A = \frac{\Phi_A}{\Phi_o}, \quad B = \frac{\Phi_B}{\Phi_o}, \text{ and } T = \frac{\Phi_T}{\Phi_o}. \tag{7}$$

The absorption coefficient, a, is the absorptance per unit distance in the layer, Δr:

$$a = \lim_{\Delta r \to 0} \frac{A}{\Delta r} = \lim_{\Delta r \to 0} \frac{1}{\Delta r} \frac{\Delta \Phi}{\Phi} \tag{8}$$

where $\Delta\Phi = \Phi_A$, the loss of radiant flux over distance Δr, due to absorption (Φ_o - Φ_T, for a non-scattering medium), and which in the limit yields:

$$\int_0^r a \, \mathrm{d}r = \int_{\Phi(0)}^{\Phi(r)} \frac{1}{\Phi} \, \mathrm{d}\Phi \tag{9}$$

where $\Phi(0)$ is the incident flux and $\Phi(r)$ is the radiant flux measured at r (Φ_T). The absorption coefficient, with units of m^{-1}, is given by:

$$a = \frac{-1}{r} \log_e \frac{\Phi(r)}{\Phi(0)} \ . \tag{10}$$

where $\Phi(0) = \Phi_o$. This equation yields two important pieces of information, first that the absorbed radiant flux is a function of path length (the longer the path, the greater the loss of radiant flux to absorption) and second, that the radiant flux decays exponentially along that path, a fact discussed in (Morel, 2005).

Thus, in a scattering medium, the measurement of the absorption coefficient can be determined from observations of the incident radiant flux and the radiant flux that is not lost to absorption over path length r, i.e.:

$$a = \frac{-1}{r} \log_e \frac{\Phi_B + \Phi_T}{\Phi_o} \ . \tag{11a}$$

If there is no scattering in the medium, the numerator simplifies to the transmitted radiant flux, Φ_T. Similar arguments hold for the scattering and beam attenuation coefficients as well as the VSF:

$$b = \frac{-1}{r} \log_e \frac{\Phi_A + \Phi_T}{\Phi_o} \tag{11b}$$

$$c = \frac{-1}{r} \log_e \frac{\Phi_T}{\Phi_o} = \frac{-1}{r} \log_e T \tag{11c}$$

$$\beta(\bar{\theta}) = \frac{\int_{\varphi_1}^{\varphi_2} \int_{\theta_1}^{\theta_2} \beta(\theta') \sin\theta' \, \mathrm{d}\theta' \, \mathrm{d}\varphi'}{\int_{\varphi_1}^{\varphi_2} \int_{\theta_1}^{\theta_2} \sin\theta' \, \mathrm{d}\theta' \, \mathrm{d}\varphi'} = \frac{-1}{r\Delta\Omega} \log_e \frac{\Phi_o - \Phi_{B'}}{\Phi_o}, \text{ and } \Delta\Omega \equiv \int_{\varphi_1}^{\varphi_2} \int_{\theta_1}^{\theta_2} \sin\theta' \, \mathrm{d}\theta' \, \mathrm{d}\varphi' \ . \tag{11d}$$

Eqn. 11c indicates that the beam attenuation coefficient is theoretically related to the transmittance, T. However, because T is a relative quantity, it is usually reported as a percentage and reported with the path length over which it was measured (i.e. 77% transmission in a 25 cm path, relative to water). The integral on the left of the equal sign in eqn. 11d is the scattering coefficient within a solid angle ($\Delta\Omega$) defined by the ranges θ_1 to θ_2 and φ_1 to φ_2, and $\Phi_{B'}$ is the scattered radiant flux integrated over all angles except for the solid angle defined by the range θ_1 to θ_2 and φ_1 to φ_2.

The key to accurate measurements of these IOPs is the capability to configure instrumentation such that the appropriate radiant flux components are accounted for. The key to accurate interpretation of these IOPs with respect to biogeochemical information is in part dependent upon the resolution and limitations of in situ IOP measurement and in part dependent upon the sensitivity of the measured coefficients to variations in the biogeochemical properties.

One theoretical tool used to study the interaction of light and matter is Mie theory, which yields the IOPs associated with monochromatic light impinging on a homogeneous sphere of a given size and complex refractive index (Mie, 1908). The real part of the index of refraction indicates how the speed of light changes between the particle and the medium while the imaginary part is proportional to the wavelength times the absorption of the material (e.g. van de Hulst, 1957; Chapter 4, Appendix II, Morel, 2005). Such modeling has been found to be very useful in interpreting in situ IOPs (e.g. Morel, 1973; Gordon, 1974; Twardowski et al., 2001) as well as predicting IOPs for which no measurement was available (e.g. backscattering in Stramski and Kiefer, 1991). It is noteworthy, however, that the limitations imparted by the assumption of sphericity (Bohren and Hufmann, 1983) and homogeneity (Bricaud et al., 1992; Kitchen and Zaneveld, 1992; Zaneveld and Kitchen, 1995) have not been fully investigated for oceanic particles.

Throughout this manuscript we will assume a simple theoretical size distribution of idealized particles given by a power-law (sometimes referred to as hyperbolic or Junge-like) function, described by:

$$N(D)\,\mathrm{d}D = \mathrm{C}_N\,D^{-\xi} \qquad (12)$$

where D is diameter (m), $N(D)$ is the number of particles per volume in the interval between D and $D + dD$ (particles.m^{-3}.μm^{-1}), C_N is a constant proportional to the particle concentration (particles.m^{-3}) and ξ is the power-law slope (dimensionless). Eqn. 12 has been found to capture much of the first order variability observed in oceanic particles size distributions for the range of particles most likely to impact the IOPs (Bader, 1970; Morel, 1973; and see discussion in Stramski and Kiefer, 1991 and Twardowski et al., 2001), although this cannot be verified for particles below ~0.5 μm, due to the difficulty in detecting them with routine instrumentation. One example where the power-law distribution is not a good approximation of the oceanic particle size distribution (PSD) is during monospecific algal blooms when the algal cell size distribution is better predicted by a Gaussian or lognormal distribution and this distribution skews the total PSD away from the power-law shape. In two illustrative examples below we will superimpose a Gaussian population of phytoplankton on top of a background hyperbolic distribution (e.g. Bricaud et al., 1995) to demonstrate the impact of a bloom on IOPs.

5.3 IOP measurement reality

It should be stated up front that it is *impossible* to measure the IOPs as defined theoretically in the previous section due to errors incurred by physical and electronic limitations in instrumentation; for example, transmitted photons cannot be detected in the absence of far forward scattered photons because of the limitation on the size of the detector solid angle. That said, IOPs can be estimated with significant accuracy with proper instrument characterization, and corrections for the limitations. The instrument elements of interest are the source beam, the sample compartment or interrogation volume, and the detector, the configurations of which determine which IOP is being measured and what corrections have to be applied (e.g. Bricaud et al., 1995, Mueller et al., 2003).

5.3.1 Beam attenuation coefficients measured with *c*-meters (transmissometers)

The ideal instrument configuration for measuring the beam attenuation coefficient should meet a number of criteria so that the measurement follows the theoretical constraints. The source beam should be comprised of a plane wave such that all photon rays are traveling parallel to one another. The beam width should be as small as possible relative to the instrument length (Tyler et al., 1974), yet large relative to the detector field of view to avoid edge effects. The geometric

path length should be of an appropriate length for the water type so that the sample is optically dilute (i.e. in which multiple scattering is negligible, for example a 5-cm path for turbid coastal waters and a 25-cm path for clear oceanic waters). The detector should have an infinitely small acceptance angle to exclude far-forward scattered light. While most of these configuration constraints can be achieved, there are physical limitations to the detector acceptance angle and thus some portion of the forward scattered beam is collected as transmitted flux. The magnitude of this error is a function of the acceptance angle of the detector and the shape of the volume scattering function for the medium. In the ocean, the volume scattering function undergoes the greatest rate of increase with decreasing scattering angle (e.g. far forward scattered light; Figure 5.5) and thus this error can be very significant, as will be demonstrated below, and instrument-to-instrument comparisons of beam attenuation can be very problematic if they have different detector geometry (Voss and Austin, 1993; Pegau et al., 1995).

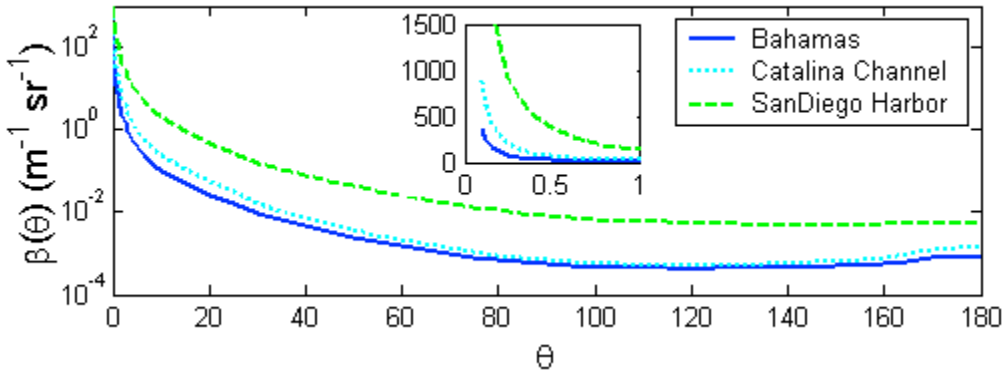

Figure 5.5. Volume scattering functions (VSFs) observed for natural waters from three optically-diverse environments: clear open ocean Bahamas, coastal Catalina Channel, and turbid San Diego Harbor (data from Petzold, 1972). Inset shows the VSFs for the first degree of forward scattering on a linear scale. Beam transmissometers have finite acceptance angles that capture this far forward scattered light and attribute it to unattenuated flux.

Here we consider some *c*-meter examples: the AlphaTracka, the Sequoia LISST (Laser In Situ Scattering and Transmissometer) and the WET Labs ac-9and c-star (the nine and single wavelength versions, respectively) (Table 5.1). The configurations of the instruments are quite different and thus quantitative comparisons yield large differences with respect to magnitude, but will yield similar qualitative or relative results, assuming no change in particle size distribution (PSD). The degree of accuracy and the need for correction depend upon whether the derived beam attenuation coefficient is being used for radiative transfer modeling (Gordon, 1993) or for

the detection of suspended particulate matter. In the former case, calculation of the radiance distribution requires very high accuracy in the derived IOPs while calculations of irradiance, reflectance and diffuse attenuation are insensitive to small variations in the acceptance angle of beam attenuation. The sensitivity required for the detection of particulate matter will be explored further in this chapter. As a rule, however, beam attenuation coefficients should always be reported with configuration information, particularly the detector acceptance angle. The difference in the derived beam attenuation coefficients for natural waters can be as high as 15% between the ac-9 and the LISST (for particles with a refractive index of 1.05 + i0.001 and a size distribution approximated by a power-law with a slope of 4). The instrument with the smallest detection angle, the LISST, yields the largest *c* coefficient, and yet even this instrument can significantly underestimate the theoretical beam attenuation coefficient. However, utilizing a single instrument, the relative estimates of the beam attenuation coefficient can be very powerful with regards to detecting the magnitude and variability of suspended particulate material. The differences between instrumentation are attributed to trade offs between size, weight, spectral resolution, power and the needs of the targeted user.

Ideally the optical path length (i.e. the distance that photons travel between source and detector) is equal to the geometric path length of the sample compartment, so that all of the photons that reach the detector are unscattered. In optically thick media, photons can undergo multiple scattering. In this case the optical path length of the multiply-scattered photon exceeds the geometric path length (Figure 5.6), thus photons have a greater probability of being scattered or

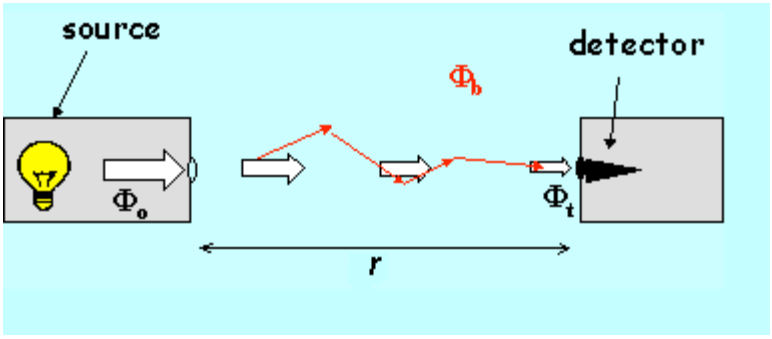

Figure 5.6. Conceptual diagram of the radiant flux in a beam transmissometer in which incident flux, Φ_o is multiply scattered (red arrows, Φ_B) or transmitted (white arrows, Φ_T) into the detector. In this case the geometric path length, *r*, is smaller than the optical path length for some photons, described by the sum of the red arrows.

absorbed, a process that leads to an overestimated attenuation coefficient. Conversely, some portion of the multiply-scattered photons can enter the detector, appearing unattenuated, a

process that leads to an underestimated attenuation coefficient. These are difficult phenomena to correct for (van de Hulst, 1957) and it is best to control the optical thickness of the measurement by controlling the geometric path length (i.e. choosing a shorter path length instrument for more turbid waters) so that the instrument response is linear with particle concentration. A rule of thumb suggested by van de Hulst (1957) to ensure single scattering, is to maintain the configuration such that the product $cr < 0.1$ (where r is the geometric path length). This criterion is very restrictive and was determined analytically using a VSF for molecular suspension (which are very flat in the forward angles). The VSFs for aquatic particles tend to be much more peaked in the forward direction (Figure 5.5) and thus the criterion can be relaxed. The criterion for a specific environment can be determined by measuring the IOPs of a dilution series of the particles under consideration and quantifying the range of linear response of the IOP versus particle concentration. Indeed, we observe the response of beam transmissometers to be linear with concentration even for $cr \sim 1$.

5.3.2 Absorption coefficients measured with the ac-9

Currently there is only one commercially available in situ absorption meter that measures absorption based upon eqn. 11a (Zaneveld et al., 1990; Moore et al., 1992). Other instrumentation exists to derive absorption from hybrid or apparent optical properties, but these approaches will not be treated here. Absorption measured with the WET Labs ac-9 is similar to a beam attenuation measurement, with the exception that the configuration is optimized to collect scattered light (Figure 5.7), the majority of which, for natural particulate populations, will be in the

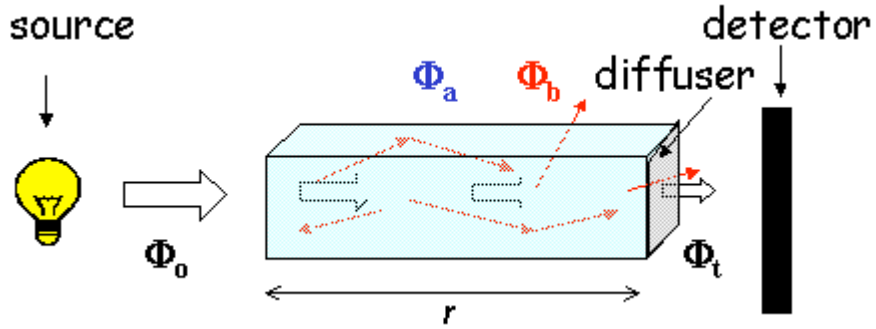

Figure 5.7. Conceptual diagram of the radiant flux in a reflecting tube absorption meter in which incident flux is absorbed, transmitted, scattered into the detector, reflected off the side walls into the detector, scattered out of the cuvette, or multiply scattered.

forward direction. This is achieved through a quartz sampling tube, which reflects forward scattered light back into the sample path, and a diffuser in front of the detector to collect the

forward scattered light. However, not all of the scattered light is collected, and from equation (11a) it is clear that the amount of scattering that is not detected leads to a direct overestimation of the absorption coefficient by attributing scattered flux to absorbed flux. It is that portion of the scattering function that is approximately > 40^o (i.e. the back- and side-scattered light) that is not detected (Kirk, 1992). Scattering can impact the estimation of absorption in other ways. Similar to the case for beam attenuation, when the sample is highly concentrated, the beam can undergo multiple scattering events along the path length, which increases the probability of absorption, leading to overestimation. These errors can be corrected to varying degrees of accuracy depending upon the availability of ancillary data (section 5.4).

5.3.3 Scattering coefficients

Scattering coefficients, measured according to eqn. 11b are difficult to quantify due to the near impossibility of independently detecting the absorbed flux (c.f. an instrument that measures scattering directly has recently been designed, e.g. Musser et al., 2004). For these reasons, scattering coefficients are generally derived by difference between the measured beam attenuation and the absorption coefficients (eqn. 3). In the absence of independent estimates of absorption, the scattering coefficient can be derived from the beam attenuation coefficient at a wavelength for which absorption by dissolved and particulate materials is negligible (e.g. 650 nm to 660 nm or in the near infrared > 720 nm, depending upon seawater composition). Thus all of the caveats for attenuation measurements apply for this approach.

There is a distinction between sensors that measure the scattering coefficient or the volume scattering function at a defined θ and φ from those that measure some aspect of scattering as a means to assess total particle concentration or total suspended load (Table 5.2). These latter sensors are often called turbidity meters or nephelometers, which express values in units of NTU (nephelometric turbidity units) or FTU (formazine turbidity units). These units are based upon a suspension of polymerized hexamethylenetetramine and hydrazine sulfate under strictly controlled conditions. These units cannot be directly converted into IOP units of m^{-1}, and are quantitatively useful only for a specific population of non-natural particles (e.g. Gibbs, 1974). So when two different brands of turbidity meters are calibrated with the same calibration suspension, they should not be expected to provide the same measurement in the natural environment because they generally have different configurations. The signals from certain of

these instruments may be converted to IOPs if appropriately calibrated for particle concentration, composition, and size distribution using appropriate calibration standards (e.g. beads of known optical properties, Zaneveld et al., 1980). Detailed knowledge of the source and detector's field of views are needed for such calibrations, but the calibrations will not necessarily apply to natural samples. These sensors tend to be more economical and if the user's application is to discern some aspect of total suspended load, such as suspended particle mass or concentration, they might provide a reasonable option compared to IOP sensors.

Measurements of the VSF or portions of the VSF are achieved with a set of divergent-beam/small-angle-detector pairs at a range of angles (e.g. Figure 5.8 for backscattering). Attenuation occurs along the path and must be corrected for, either with observations or approximations, otherwise the backscattering is underestimated by the quantity dependent on attenuation along the scattered path.

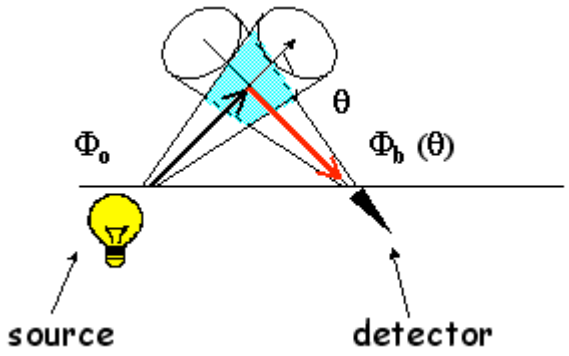

Figure 5.8. Conceptual diagram of a single angle backscattering sensor. The incident irradiance, Φ_o, is a divergent beam with a known solid angle (bold arrow), the detector, likewise has a known detection solid angle. The detected scattered flux, Φ_B (bold red arrow), occurs about the central backscattering angle, θ, within a volume (cyan) defined by the intersection of the incident and detected solid angles. The geometric path length is defined by the sum of the geometric lengths of the bold arrows. Simplified from Maffione and Dana (1997).

Complete VSF measurements are not routinely made and there is no commercially available instrumentation as of yet, although some are likely in the next 5 years. Selected in-situ VSF observations made with the General Angle Scattering Meter (GASM) in the early 1970's (Petzold, 1972) are still used today in radiative transfer modeling because of the dearth of publicly-available VSF observations. GASM resolved the VSF at 1^o resolution from 10^o to 170^o and at 532 nm. New technology (Lee and Lewis, 2003) has an angular resolution of 0.3° at a single wavelength, but is not yet commercially available.

The backscattering coefficient is currently determined from one or more measurements of the VSF at $\theta > 90^o$. A single angle measurement of the backscattering has been found to be significantly related to the integrated backscattering coefficient (Oishi, 1990; Maffione and Dana, 1997; Boss and Pegau, 2001) (Figure 5.9A). The exact angle that minimizes the error

depends upon whether the instrument is calibrated relative to pure water or to a solid calibration standard (e.g. for the WET Labs and HOBI Labs instruments, respectively) (Boss and Pegau, 2001). When the backscattering is measured at multiple angles (e.g. 3, as is the case the WET Labs ECO-VSF), the backscattering coefficient is computed, via eqn. (5), by integrating the function $\beta \sin\theta$ over $\theta = \pi/2$ to π. Since the observations are only made at 3 angles (110°, 125° and 150°), a polynomial is fit to those three data points. Noting that the $\sin(\theta = \pi) = 0$, a fourth point at 180° can be included for a total of 4 points in the polynomial fit (Figure 5.9B). A third order polynomial is the lowest order polynomial providing the best fit to the VSF in the backward direction (M. Twardowski, pers. comm.); higher orders do not increase significantly the fit.

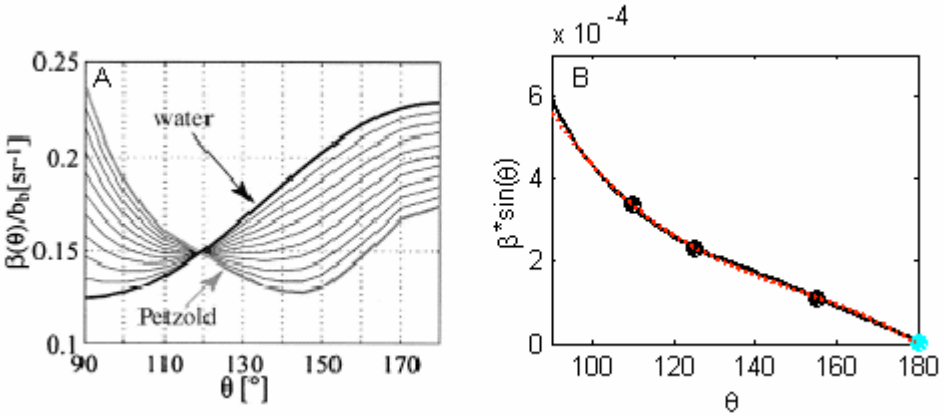

Figure 5.9. A. Relationship between the normalized volume backscattering function and backscattering angle for a range of volume scattering functions from pure water to Petzold's San Diego Harbor (see Figure 5) (from Boss and Pegau, 2001). The angle at which they intersect is ~117°. B. Graphical representation of the calculation of the backscattering coefficient from three point observations at discrete angles as in eqn. (5), the integration of the product of the volume scattering function, β, and the sin of the scattering angle, θ, shown here for a typical oceanic VSF (black). Observational detection angles of the WET Labs VSF meter (black symbols), and the data point at 180° (cyan symbol), which is necessarily zero because $\sin(180^o) = 0$. A third order polynomial fit to the four data points (red) is used in the integration over θ to determine the backscattering coefficient.

5.4 Calibrations, characterizations and corrections

5.4.1 Absolute calibrations, biogeochemical calibrations, tracking

Each commercially-available IOP instrument undergoes careful absolute calibration procedures to convert the detected analogue or digital signal into IOP units (e.g. m^{-1} or $m^{-1}.sr^{-1}$, see

discussion in Cullen and Davis, 2003). Often included in these calibrations are the processing steps required to account for the errors associated with non-ideal configurations. In other applications these steps may require separate processing by the user. A second order calibration may also be applied, either by the factory, or by the user, in which either the signal or the derived IOP is related to some scalar biogeochemical property or concentration such as total suspended solids, particle concentration or chlorophyll concentration. These calibrations are generally based upon many more assumptions, the details of which will be covered in Chapter 7 (Sosik, 2005). Finally, ancillary calibration procedures may be employed, not to derive absolute IOP units but to track changes in the instrumentation between absolute calibrations. This tracking procedure might be necessary in situations of long deployments, cruises or experiments when absolute calibration might be difficult (calibration standard difficult to obtain) or impossible (in situ deployment). This type of tracking might be done by looking at the time series of the dark signal or air calibration. The configuration of the instrument, the suite of corrections and the absolute calibration are what determine good quality quantitative observations from qualitative or uncalibrated ones. There are many instruments available, all with techniques for corrections and calibrations; however, understanding the sensitivity and robustness of the observations is necessary for obtaining optical observations that translate into IOPs which are comparable between sampling dates, between instruments, and between investigators.

Absolute calibration requires some sort of reference material either to obtain a known signal (i.e. a scattering surface of known reflectance used to calibrated the scattering sensors) or to obtain an absolute signal relative to the reference for which the IOPs are known (i.e. relative to a pure water reference). Independent means of assessing the purity of the calibration material is vital for obtaining accurate absolute calibrations. For example, a Spectralon® plate, with known reflectance, does degrade with time and exposure to light, and optically pure water can be problematic to make and maintain, even in the laboratory, due to its high reactivity with other substances and its tendency to form highly scattering micro bubbles.

Ideally, instruments should be calibrated by the factory before and after each usage. Practically, however, this may not be possible and the user must develop an independent calibration and tracking protocol. Unavoidable sources of instrument variations with time include changes in lamp output magnitude and spectral dependence, detector degradation and response, and filter degradation and response. With careful protocols, these can be tracked and quantified

and the data can be corrected. Avoidable sources of instrument variation include dirty instrumentation, incorrect configurations, and inappropriate blanks. Often these are not quantifiable and accurate data can never be recovered (Cullen and Davis, 2003). A sample observational protocol for an ac-9 is as follows:

1. Obtain factory air and pure water calibration
2. Clean instrument tubes and optical windows with ethanol and lens paper
3. Perform air and pure water calibrations on the bench top with instrument in a vertical position, using the appropriate factory calibration. Values should be within instrument specifications of zero.[5]
4. Place instrument in its deployment configuration (i.e. strapped to cage or frame). Repeat steps 2 and 3. The air and pure water calibrations should be within factory specifications of those derived in step 3. If not, check that the optical alignment has not been changed by deployment configuration (it is recommended that only one end of the instrument is tightly strapped so as to prevent bending).
5. Repeat steps 2 and 4 daily during observational program, if possible, noting the potential difficulty in obtaining absolute calibrations.
6. Perform a final air and pure water calibration and compare them to the pre-deployment values (when confident about laboratory setup, pure water facilities and procedures), otherwise obtain factory air and pure water calibration post deployment. Explain why a factory air calibration (and water) could be better than doing it yourself. What's the difference?
7. If post-deployment calibrations are significantly different from pre-deployment values, analyze the time course of air and pure water calibrations to quantify drift or step-functions in instrument response. If deployment does not permit a time course of pure water or air calibrations, as shown in Figure 5.10, examine the raw data for features consistent with a step

[5] A newly calibrated instrument should ideally measure the absorption and attenuation of pure water within the instrument specifications (e.g. ± 0.005 m^{-1}). However, calibrations are very sensitive to instrument position and some changes may occur in transit. If only one wavelength is significantly different from the calibration (i.e. > 0.1 m^{-1} in both *a* and *c*), this may indicate a filter malfunction. When *a* and *c* measurements at all wavelengths are significantly different from zero, this may indicate a detector or lamp malfunction. Checking for stability over the course of a few days may indicate that the instrument underwent some drift in transit and that the new pure water calibration, performed in your laboratory, is necessary. Over longer time scales the ac-9 calibration does change as a function of time (Order 0.02 m^{-1}/200 days) Twardowski et al., 1999), and care must be made to do periodic calibrations to keep track of this drift.

function or trend. Using the pre- and post-calibration values, construct an appropriate time course of factory calibration to apply to in situ data (Figure 5.10).

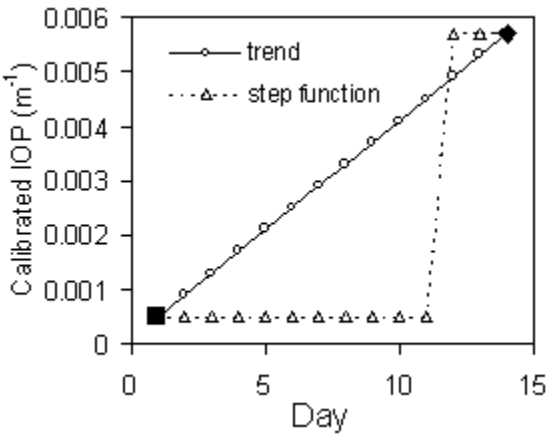

Figure 5.10. Hypothetical time course in pure water IOP observations relative to pre-deployment factory calibration. An observed linear trend between pre- (filled square) and post- (filled diamond) deployment factory calibration is given by circles, a step function is given by triangles. These daily observations would indicate how to apply factory calibrations to deployment observations during post-processing: a linear interpolation between the pre- and post deployment calibrations or the pre-deployment calibration until day 11 and the post-deployment calibration from day 12 through day 15.

5.4.2 Environmental sensitivity

Electronic instrumentation often exhibits sensitivity to ambient temperature. Optical instruments that depend upon precise alignment may also exhibit sensitivity to ambient pressure. While these are often well characterized or controlled by the factory, it is a source of potential variability that is worth verifying as there may be some residual effects. The severity of this error depends upon the deployment platform. Profiling instruments that pass through a sharp thermocline, or profile to great depths are more likely to yield problematic data because of the mismatch between the profiling speed and the time for the instrument to reach thermal equilibrium. These artifacts can be quantified with careful characterization in the laboratory and can become part of the data processing sequence as long as time-dependent hysteresis is not significant or profiling speeds are very slow.

A second order of environmental sensitivity is that of the reference or calibration material. For example pure water absorption and scattering properties are both temperature and salinity dependent and this dependence has been well quantified (Morel, 1974; Pegau and Zaneveld, 1993; Pegau et al., 1997). Therefore, a factory calibration with 25 C pure water will not be the same as a calibration with 10 C pure water, nor would the calibration for 33 psu water be the same as that for pure water. Thus, the dependence of the reference material IOPs on temperature must be quantified in addition to the instrument response to temperature (i.e. the dependence of the pure water running through the sample compartment or the sample volume

and the dependence of the instrument *in* water of a temperature different from room temperature). Generally the variations in water optical properties as a function of temperature are at specific wavelengths associated with the harmonic absorption features of water (most notably ~600 nm, ~665 nm, and ~740 nm), while the instrument-dependence will be different at all wavelengths depending upon instrument electronics and the thermal properties of the instrument material.

5.4.3 From raw data to calibrated and corrected in situ IOPs, an example with the ac-9

An example of the steps required to derive accurate IOPs from ac-9 observations is given in this section. It is often difficult to discern problematic data from real-time profiles or time series observations at a single wavelength, thus it is recommended that the user examine the spectral data in real-time as well. All raw data are binned such that each bin represents an independent observation as follows. The flow tube residence time is determined by measuring the volume of the flow tubes and the flow rate through the tubes. The latter can be performed in the field or in the laboratory with the instrument and pump connected; collect the outflow from the sample tubes, noting the time of the collection. Calculate the flow rate from the quotient of the volume collected and the time of the collection. Knowing the sampling rate of the instrument (6 Hz) one can determine how many realizations must be binned to derive an independent observations in situ. Using a SeaBird pump in the field typically requires binning approximately 6 realizations (depending upon the pump settings), using restricted gravity flow in the laboratory typically requires binning approximately 36 realizations. These computations are critical for observing fine scale features in the field so as to prevent the signal from a large anomalous particle to be interpreted as a "thin layer". Additionally, binning reduces the error associated with the fact that different parcels of water flow through the absorption and attenuation tubes. All of the following calibrations and corrections are performed on binned data only.

In the following example, a profile of beam attenuation and absorption was measured in stratified coastal waters. The raw observations, calibrated relative to pure water with the pre-deployment factory calibration, do not provide any evidence or problematic data (Figure 5.11 A, B). However, examination of the spectral values at discrete depths indicates that the pre-deployment calibrations may not be accurate (Figure 5.11 C, D, symbols). The expectation is that the spectral attenuation is a smoothly-varying function (i.e. the 555 nm channel is anomalous)

and that the absorption resembles an exponential function associated with NAP or CDM with or without the impacts of phytoplankton pigments (again the strong dip at 555 nm is not characteristic of either; note that the calibration errors do not necessarily have to occur at the same wavelengths for *a* and *c* as they do in this case if the problem is related to the detector or sample tubes). Note that if only the surface spectra displayed this spectral irregularity, and it was not consistently at the same wavelengths, bubbles might be suspected. Application of current calibration coefficients (derived from shipboard calibrations or from pre- and post-deployment factory calibrations as in Figure 5.10) result in spectral coefficients that behave as predicted (Figure 5.11C, D, black lines).

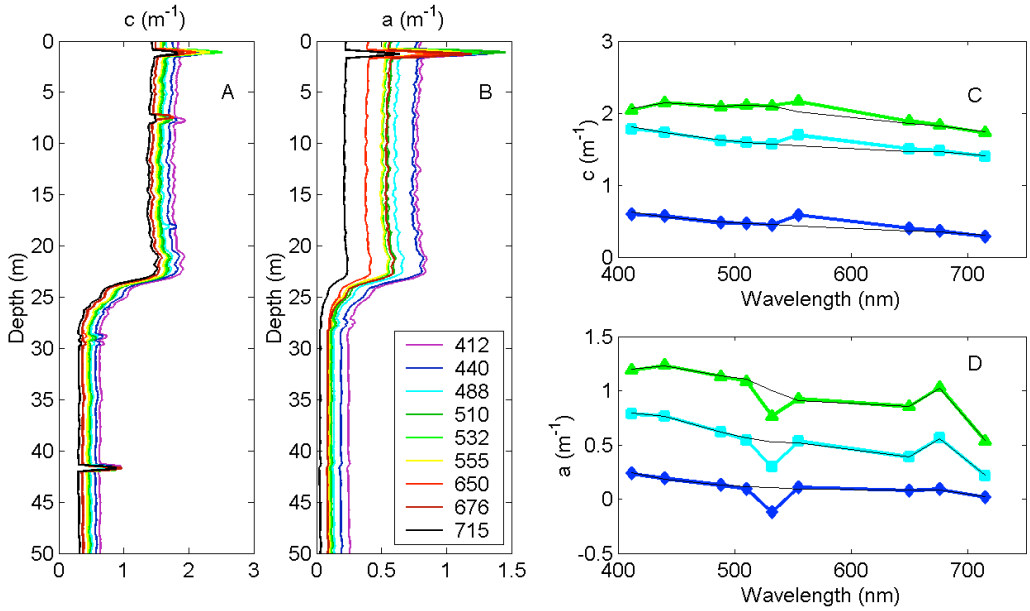

Figure 5.11. Example of observed attenuation and absorption measured with an ac-9 in stratified coastal waters. Depth profiles of raw attenuation (A) and absorption (B) observations using a pre-deployment factory calibration at 9 wavelengths. Attenuation and absorption spectra (C and D, respectively) taken from discrete depths within and below the mixed later and at the 2 m absorption peak. Spectra corrected for post-deployment calibrations shown in black lines.

After the appropriate calibrations are applied to the observations, absorption and attenuation must be corrected for variations in the absorption by pure water due to differences between the temperature and salinity of the in situ water and that used in the factory or laboratory calibrations. Using the algorithms of Pegau et al. (1997), the corrected spectra are obtained (Figure 5.12A, shown for absorption only). In this case the in situ water was more saline and colder than the pure water used to calibrate the instrument (0 psu and ~25 C). This

correction is applied to both the absorption and attenuation coefficients over the visible spectrum, although for this particular filter configuration, only the values at 715 nm exhibit

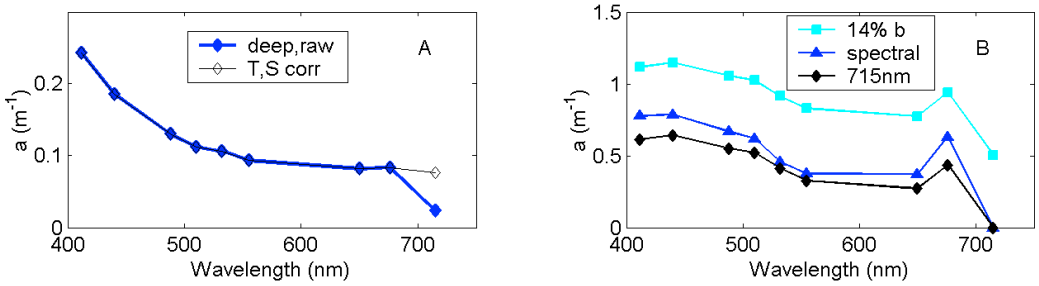

Figure 5.12 A. Absorption spectrum from the deep layer, as in Figure 5.11D, before and after temperature and salinity correction (blue square and black triangles, respectively). B. The absorption spectrum from the absorption peak in Figure 5.11D, after applying post-calibrations and temperature and salinity corrections, corrected for scattering by three different models. See text for details.

significant effects. This correction is especially critical for the absorption observations because some scattering correction schemes hinge on the observed value of absorption at 715 nm (Zaneveld et al., 1994) and thus any error due to temperature or salinity will propagate to the scattering correction.

In the absence of synchronous CTD measurements with IOP measurements, an accurate temperature correction can be obtained using the spectral attenuation measurements alone. The spectral behavior of beam *c* has been well documented to be a smoothly varying function of wavelength for multispectral measurements with wide spectral windows around each wavelength (Voss, 1992; Boss et al., 2001a). Similar to the spectrum for absorption shown in Figure 5.12A, the 715 nm value falls away from the curve described by the other 8 wavelengths. Using a power-law spectral fit to the 8 wavelengths of observed beam *c*, the value at 715 nm can be predicted. The difference between this predicted value and the observed value is the correction in *a*(715) due to temperature and salinity variations. This can then be used to correct the observed absorption spectrum (and, interestingly, the in situ temperature can be determined from the absorption correction).

The final step is the scattering correction applied to the absorption observations to account for the losses due to scattering out of the detector (Figure 5.7). There has been no consensus on how to correct the absorption for scattering losses (Kirk, 1992; Zaneveld et al., 1994; Bricaud et al., 1995; Roesler, 1998). Methods range from subtracting the observed offset

in the absorption at 715 nm, consistent with that done in spectrophotometry (Babin and Stramski, 2002), to subtracting a percentage of the spectral scattering coefficient. Below are three models for scattering correction:

$$a(\lambda) = a_{meas}(\lambda) - a_{meas}(715) \quad (13a)$$

$$a(\lambda) = a_{meas}(\lambda) - n\%*(c(\lambda) - a_{meas}(\lambda)) \quad (13b)$$

$$a(\lambda) = a_{meas}(\lambda) - a_{meas}(715) * \frac{c(\lambda) - a_{meas}(\lambda)}{c(715) - a_{meas}(715)} \quad (13c)$$

where $a(\lambda)$ is the scattering-corrected spectral absorption, $a_{meas}(\lambda)$ is the measured spectral absorption, after calibrations and temperature-salinity corrections have been applied, and $c(\lambda)$ is the measured spectral attenuation after calibrations and temperature-salinity corrections have been applied. It is clear that the nature of the scattering correction is critical to interpretation of the spectral absorption coefficients (Figure 5.12B).

Both the 13a and 13c scattering corrections imply that there is no non-water absorption at 715 nm. Babin and Stramski (2002), using an integrating sphere and spectrophotometry, conclusively demonstrated that there is minimal absorption at 715 nm by particulate material, including inorganic particles, in a range of natural waters. This suggests the observed signal $a_m(715)$ is due to scattering alone and that the absorption at 715 nm should be zero. This would indicate that the percent of b correction (eqn. 13b) is not appropriate because it results in a non-zero value for absorption at 715 nm, and further suggests that a constant percentage of the scattering is lost to the detector, when instead this percentage would strongly depend on the angular dependence of the VSF[6]. That leaves the spectrally independent and spectrally dependent corrections (13a and c, respectively). Observations and modeling of the optical properties of both weakly and strongly absorbing particles (see Stramski and Mobley, 1997 compilations) indicate that scattering is spectrally dependent except for extreme cases of large polydispersed (varied size distribution), weakly absorbing particles in which b is spectrally flat. The model given by 13c, which essentially removes a fraction of the spectral scattering, scaled to the measured absorption at 715 nm, accounts for both types of particles. The error in 13c is that portion of the

[6] Some authors suggest that there is non-zero absorption in the range of 715 nm, although methodological errors might explain their observations. If this is found to be true in the future, additional work on scattering corrections will be necessary as attributing all the $a(715)$ signal to scattering will lead to underestimated absorption coefficients.

scattering losses that are due to backscattering. For some strongly absorbing particles, the spectral shape of the backscattering may be different from the spectral shape of total scattering. However, based a few studies and data sets, the spectral backscattering to scattering ratio seems to be relatively independent of wavelength in natural waters (e.g. Ulloa et al., 1994; Twardowski et al., 2001).

5.5 Instrument sensitivity to particle characteristics

Interpretation of observed IOPs with respect to the underlying biogeochemical properties of oceanic substances requires an understanding of how the IOPs vary in response to changes in particle properties and how accurately instrumentation resolves those changes. In this section, we simulate IOP variability as a function of particle concentration, composition (as revealed by the real refractive index), and size distribution (Bricaud et al., 1986). We end with a simulation of the development of two algal blooms of two very different algal species. In the first set of these simulations, we compute the volume scattering function for populations of spherical particles that have defined concentrations, defined refractive indices, and sizes which are assumed to obey power-law particulate size distributions with defined slopes, ξ (Figure 5.13)[7]. Except in the case of examining the response to particle concentration, the simulated volume scattering functions have been normalized to the integrated particle volume, thus removing the biomass effects on the observations. We then compute the beam attenuation coefficient that would be observed by two commercially-available instruments, the Sequoia LISST and the WET Labs ac-9. In general, as particle concentration increases, the absorption, scattering and attenuation coefficients increase, and if all else is held constant, they increase linearly with concentration. This provides the robust approach to estimating particle or dissolved concentrations with IOP measurements. Particle attenuation and scattering also increase as the index of refraction increases, which is the basis for

[7] A specific note about microbubbles in the aquatic environment: it has been suggested that such bubbles are responsible for significant brightening of ocean color radiance as measured by satellite and airborne sensors because the backscattering by particles cannot seem to account for the predicted backscattering coefficient derived from ocean color (see discussion in Stramski et al., 2004). The IOPs of microbubbles can be modeled very accurately using Mie theory (Zhang et al., 1998) as they are homogeneous spherical particles with size distributions predicted from wind speed and a known index of refraction relative to water of 0.75. However, measuring the IOPs of microbubbles is not trivial. First because the presence of a ship may artificially introduce bubbles into the surface layer and second because any manipulation of the sample, such as drawing it through a sample chamber, as in the case of an ac-9, can modify the natural population. Flat face sensors such as the Hydroscat and ECO-series sensors provide the most robust means to sense natural bubble populations. Bubbles are not included in the following simulations.

using IOP measurement to estimate particle composition. Finally, particle IOPs are significantly influenced by particle size distribution, but not in predictable or linear manner. In section 5.5.7 we address specifically which particles (in terms of size) are responsible for scattering and attenuation and thus which impact IOP measurements made with specific instrumentation.

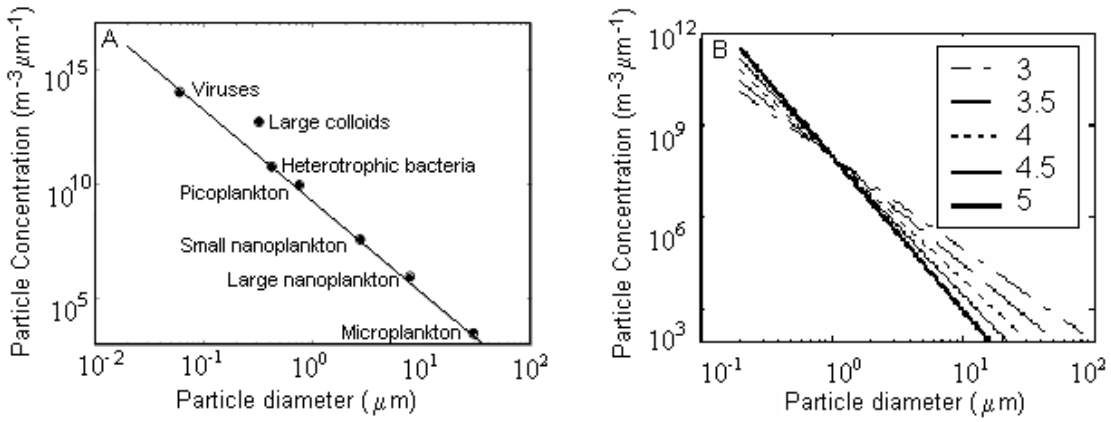

Figure 5.13. A. Size distribution for oceanic particles. Solid line represents a Junge slope of 4. Particle concentration units are differential with respect to size interval. From Stramski and Kiefer (1989). B. Range of particle size distributions as in A, for Junge slopes ranging from 3 to 5 used in simulations in the following figures.

5.5.1 IOP Measurement Sensitivity to Particle Concentration

The VSF for a population of weakly absorbing particles with refractive index of 1.05 + i 0.001, obeying a power-law size distribution (eqn. 12) with $\xi = 4$ is shown in Figure 5.14A. This would correspond to a mixed population of organic particles at any wavelength or phytoplankton at a wavelength at which they are weakly absorbing (e.g. ~555 nm or ~650 nm). The concentration values vary 50 fold on an arbitrary scale. The far-forward scattering function is shown on a linear scale in the inset. The beam attenuation coefficients that would be measured with a Sequoia LISST and a WET Labs ac-9 are within 0.05% and 5.1% of theoretical values, respectively, and the measured beam *c* is linearly related to the particle concentration (Figure 5.14B). The instrumental underestimation of beam *c* is due to the finite acceptance angles (Table 5.1), with the ac-9 exhibiting the largest underestimation due to its larger detection angle.

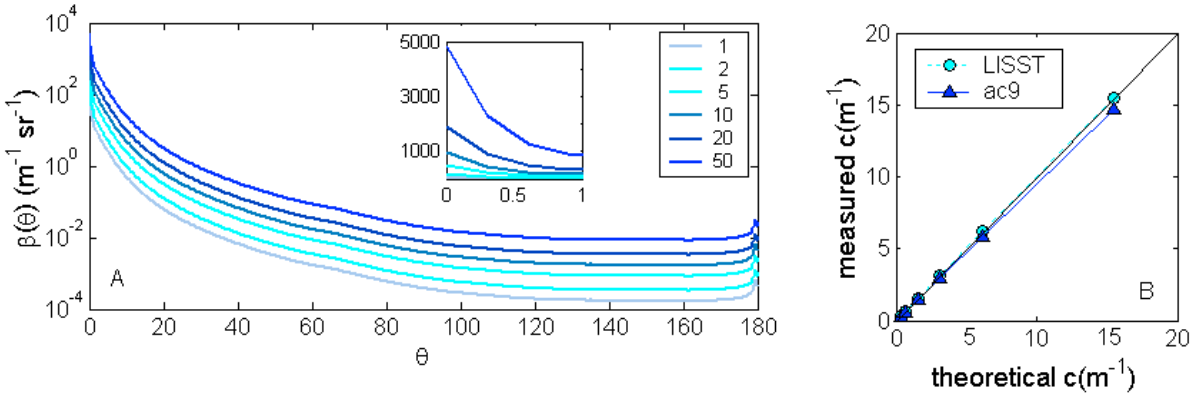

Figure 5.14. A. Volume scattering functions for a range of particle concentrations (1 to 50 arbitrary units) for particles obeying a Junge distribution with slope of 4 and a refractive index of 1.05 + i 0.001. B. Modeled values for beam attenuation coefficient coefficients for the samples in part A that would result from measurements made with a LISST and an ac-9 versus the theoretical beam attenuation coefficients, given their detection angle responses.

5.5.2 IOP Measurement Sensitivity to Composition (real refractive index)

The VSF for a population of weakly absorbing particles (imaginary refractive index of 0.001), obeying a power-law size distribution with $\xi = 4$ with real refractive indices varying from 1.01 to 1.24 is shown in Figure 5.15A. While there is a crossover in the VSF functions at approximately 0.5°, with the low refractive index particles exhibiting higher scattering at angles

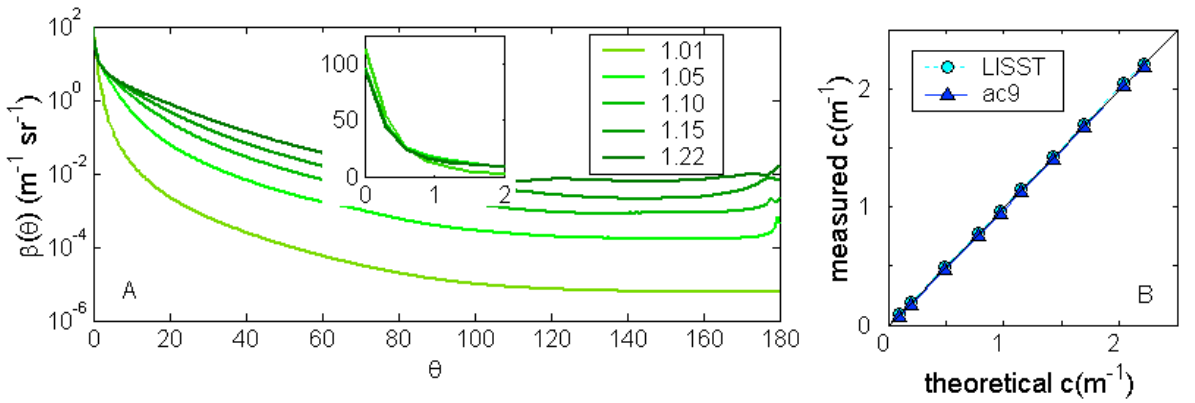

Figure 5.15. A. Volume scattering functions for particles with a range of real refractive index, obeying a Junge distribution with a slope of 4 and with an imaginary refractive index of 0.001. Curves have been normalized to total particle volume to remove the effects of biomass. Inset shows the first 2° of resolution on a linear scale. B. The beam attenuation coefficients for the samples in part A that would result from measurements made with the two instruments versus the theoretical values, as in Figure 5.14.

< 0.5°, the magnitude is not so different than the high refractive index particles. Thus for both

instruments the measured beam *c* values are within 1% of the theoretical values (Figure 5.15B). This range in real refractive index spans particles from phytoplankton to minerals, respectively, with non-algal organic particles in between (Stramski et al., 2001). As the magnitude of refractive index increases, particles are more scattering. Thus for a constant particle volume and particle size, suspended mineral particles are more scattering than organic non-algal particles, which, in turn, are more scattering than phytoplankton cells. This range in real refractive index induces more than an order of magnitude variation in the beam attenuation coefficient for a constant particle volume (so mineral particles will scatter > 10 times as much as the equivalent phytoplankton particles). This order of variation due to particle composition is comparable to that observed for a order of magnitude variation in concentration of particles with a single index of refraction. Normalizing beam attenuation by total particle volume (i.e., $m^{-1}.(m^3$ particles per m^3 of water$)^{-1}$) provides a quantity similar to the mass-specific beam attenuation and allows us to study changes in IOPs that are independent of total concentration. This clearly demonstrates that particle composition has an impact on the observed beam *c* values that are comparable to large changes in particle concentration and thus interpreting changes in the beam attenuation coefficient as purely a change in the suspended load can be significantly in error. Diel variations in cell-specific beam *c* have been observed in phytoplankton cultures and in the field. These are attributed to diel variations in the cellular refractive index caused by changes in cell composition in response to growth and division or to nutrient stress (Cullen and Lewis, 1995; Stramski et al., 1995; Stramski, 1999; Stramski et al., 2002).

5.5.3 Instrument sensitivity to particle size distribution

The particle size distribution, described by the Junge distribution function (Figure 5.13B), induces complex variations in the volume scattering function (Figure 5.16A). When the power-law PSD slope, ξ, is small, a value of 3, the particle population is comprised of a larger portion of large particles compared to a steeper slope of 5, for which the population has proportionally more smaller particles. At small angles, the VSFs exhibits a crossover between populations of particles obeying a power-law PSD slope of 3 and those obeying a power-law PSD slope of 5 (while keeping to total particulate volume or mass constant). Because both instruments collect the scattering at small angles, the curve associated with the power-law PSD slope of 4 yields the largest integral and thus the largest *c* value. Thus the magnitude of the normalized beam *c*

undergoes a non-linear change as a function of the PSD slope, whereby the attenuation is largest for particles with $\xi = 4$, and it decreases as the slope of the particle size distribution increases to 5 or decreases to 3 (Figure 5.16B). Because of the detection angle of the ac-9, such an instrument is likely to display a stronger non-linear behavior when compared to the LISST.

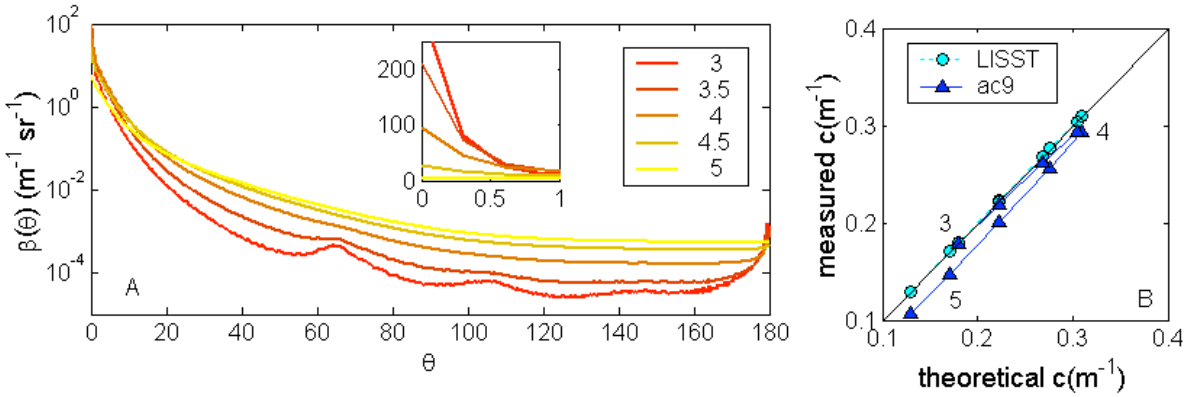

Figure 5.16. A. Volume scattering functions for particles obeying the Junge distribution with a range of slopes and with a refractive index of 1.05 + i 0.001. Curves have been normalized to total particle volume to remove the effects of biomass. Inset shows the first degree of resolution on a linear scale. Note the VSF crossover occurs in the far forward scattering, with the Junge slope of 3 (dominance by larger particles) exhibiting the strongest scattering at the smallest angles and the Junge slope of 5 (dominance by smaller particles) the strongest side and backscattering. B. The beam attenuation coefficients for the samples in part A that would result from measurements made with the two instruments versus the theoretical values, as in Figure 5.14. The values of the Junge slope are indicated, showing the hysteresis. The maximal value of beam *c* occurs at a Junge slope of 4.

The WET Labs ac-9 is currently the only commercial instrument that measures the spectral beam *c* coefficients. By removing the effects of water via the calibration procedure, and removing the effects of absorption by CDM, the particle beam attenuation, c_p, is computed. The spectral slope of particle beam attenuation is a smoothly varying function (Voss, 1992) and has been found to be well described by a hyperbolic function of wavelength (Diel and Haardt, 1980; Boss et al., 2001a; 2001b):

$$c_p(\lambda) = c_p(\lambda_o) \left(\frac{\lambda}{\lambda_o} \right)^{-\gamma} \qquad (14)$$

where λ_o is a reference wavelength, and γ is the hyperbolic slope of the spectrum. An exact linear relationship between the slope of the beam attenuation coefficient, γ, and the power-law slope of the PSD, ξ, has been demonstrated using Mie theory for non-absorbing, homogeneous

spherical particles (Volz, 1954; Morel, 1973; Diehl and Haardt, 1980) when the size distribution is considered from zero to infinity. Approximations to this relationship for limited size ranges were made by Boss et al. (2001b) such that:

$$\xi = \gamma + 3 - 0.5 \exp(-6\gamma) \quad (15)$$

where the right hand term accounts for the size range approximation. Thus a flat beam *c* spectrum ($\gamma = 0$), is associated with a small power-law PSD slope, i.e., larger particle dominance; when the beam *c* spectrum decreases from blue to red ($\gamma = 1$), this is associated with larger power-law slope or smaller particle dominance. This relationship performed well for the range of ξ found in the ocean, and for absorbing particles and non-spherical particles. This model has been successfully applied to particles in the benthic boundary layer on the continental shelf (Boss et al. 2001a) and to a monospecific algal bloom of *Prorocentrum micans* (Etheridge et al., 2002).

5.5.4 Forward Volume Scattering Function Meter Sensitivity

The Sequoia LISST is currently the only commercially available technology for measuring the volume scattering function in the forward direction (Agrawal and Pottsmith, 2000) (Figure 5.17). A collimated laser beam enters the sample chamber in which it is scattered by

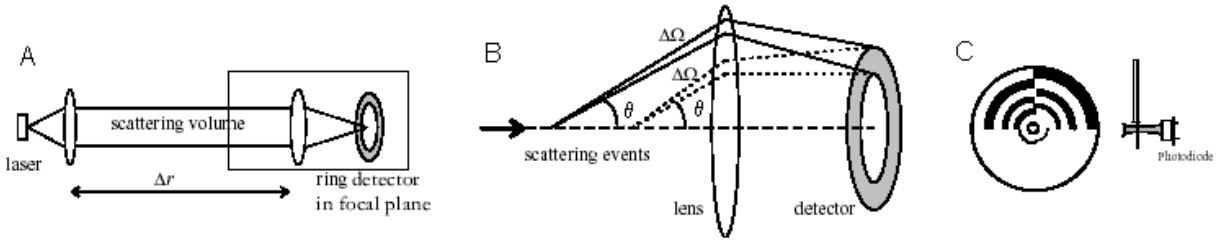

Figure 5.17. Conceptual diagrams of the Sequoia LISST, which measures the VSF in the far forward direction at 32 angular intervals. A. A laser passes through a lens into the sample compartment, called the scattering volume. B. Scattering events within the scattering volume cause photos to pass through a lens such that all scattering events along the optical path at angle θ are focused onto the detector at the same radial distance from the center of the detector, regardless of where in the sample chamber they occur. C. The detector consists of 32 concentric ring detectors arranged in quarter circle arcs, each a defined radial distance from the center and thus each associated with a unique forward scattering angle, θ. Illustrations from the LISST manual.

suspended particles. Photons are scattered at an angle θ relative to the incident direction and pass through a lens so that they are focused onto a ring detector. Photons scattered at small angles (i.e. 0.1^o) are focused at small radial distances from the center of the detector while photons that are scattered at large angles (i.e. $\sim 20^o$) are focused at large radial distances from the center of the detector. The detector is comprised of 32 discrete concentric ring detectors such that each detector receives scattered flux from discrete scattering angles relative to the incident irradiance. The discretized detection angles range logarithmically from either 0.1^o to 20^o or 0.05^o to 10^o depending upon the configuration. The detected scattered signal is dominated by diffraction rather than refraction, and the shape of the VSF is relatively insensitive to refractive index (Figure 5.15A) but very sensitive to particle size distribution (Figure 5.16A). This makes it possible to use the far forward VSF to estimate the shape of the particle size distribution for particles without accounting for their refractive index (composition). Using look up tables generated for hundreds of possible size distributions, the measured VSF is inverted to predict particle size distributions at 32 logarithmically-spaced intervals from approximately 1.25 μm to 250 μm or 2.5 μm to 500 μm, respectively (Y. Agrawal, pers. comm.). Extensive test using calibration beads (W. Slade, 2005, pers. comm.) suggests that the collimation of the laser beam does not contribute a significant uncertainty to the measurement of the near-forward VSF with the LISST (which is defined for an uncollimated beam; Figure 5.17B).

5.5.5 Backward volume scattering meter sensitivity

There are currently two major types of commercially available backscattering meters that detect within narrow angular ranges. One technology detects backscattering at a single backward angle (e.g. HOBI Labs Hydroscat and WET Labs ECObb) with multiple or single wavelength configurations (Figure 5.18). The other technology is a single wavelength sensor that detects backscattering at three angles (nominally 110^o, 125^o, and 150^o) (Figure 5.19). Multiple sensors with different wavelength light-emitting diodes (LEDs) can be used to gain spectral information. The backscattering coefficient can be derived from observations made with both of these technologies (see section 5.3.3), based upon different assumptions. The sensitivity of these instruments to particle characteristics is demonstrated in Figures 5.14 to 5.16 in the backscattering angles. To first order, the backscattering increases as the concentration of

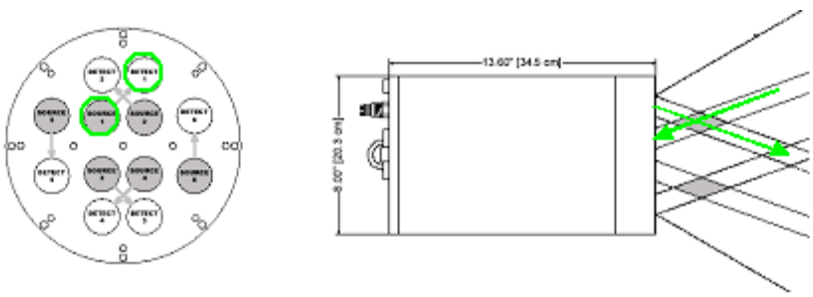

Figure 5.18. Configuration of the HOBI Labs Hydroscat 6. A. Top view of the sensor head showing 6 source/detector pairs. Source locations are shaded. Arrows indicate the associated detector location for each source. B. Side view of instrument showing the cross section of one source beam and detection field of view (arrows); associated backscattering sampling volume is in gray. Illustrations from the Hydroscat manual.

particles increases. To second order, backscattering increases as the real refractive index increases and as the imaginary refractive index decreases (i.e. weakly absorbing particles are more efficient backscatters compared to strongly absorbing particles because photons that enter particles are more likely to be absorbed and thus are not available to be backscattered), and the slope of the power-law size distribution increases (more small particles) (Stramski and Kiefer, 1991; Stramski et al., 2004). Thus variations in the backscattering signal, like the beam attenuation, are not purely a function of particulate suspended load, but also of the particle composition and size.

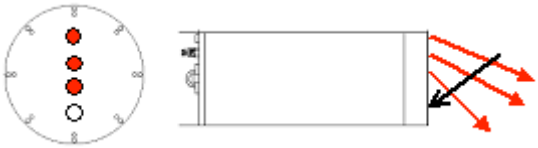

Figure 5.19. Conceptual diagram of the sensor head (left) and cross section (right) of the WET Labs ECOvsf showing the three light emitting diodes (red) and the single detector (black). The three LEDs emit light at three difference angles relative to the sensor head and relative to the single detector leading to detection of backscattering centered at 110^{o}, 125^{o}, and 150^{o}, from top to bottom, respectively. Illustrations from the ECOvsf manual.

The effects of particle characteristics on backscattering have been described by Twardowski et al. (2001) who derived the theoretical relationship between the particle backscattering ratio (essentially the efficiency of particle backscattering, given by the ratio of particle backscattering to particle scattering) and the power-law slope and real refractive index (Figure 5.20). Superimposed on the theoretical nomogram, they plotted in situ observations from the Gulf of California. Data clusters were associated with specific regions of the water column for which the dominant particle type could be identified. These particle types included algal cells (data from the subsurface chlorophyll fluorescence maximum), non-algal organic particles (from

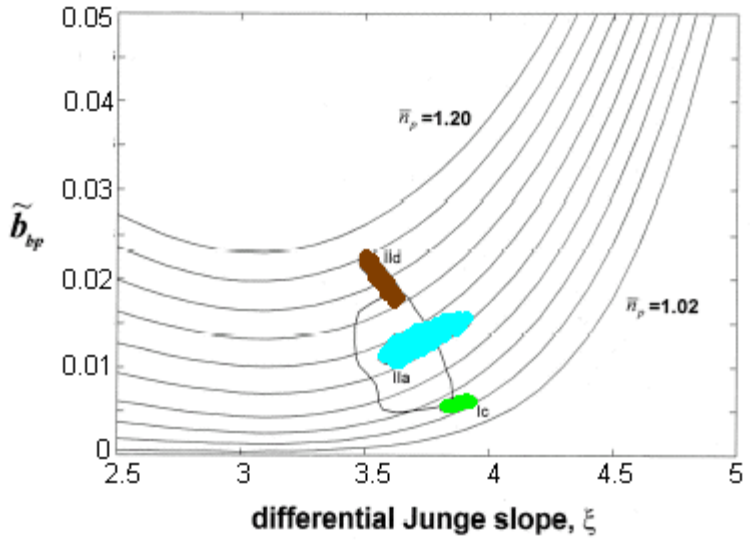

Figure 5.20. Theoretical relationship between the particle backscattering ratio and the Junge slope of particle size distribution with lines of constant real refractive index varying from 1.02 to 1.20. Superimposed are data clusters for in situ observations of particle backscattering ratio and the Junge slope (determined from c_p observations and eqns. 14 and 15), taken from the subsurface chlorophyll maximum (green), deep water column (cyan), and benthic nepheloid layer (brown). The three data clusters are dominated by algal particles, non-algal organic particles, and mineral particles, with backscattering ratios of approximately 0.005, 0.0125, 0.02, respectively. Modified from Twardowski et al. (2001).

the water column well below the euphotic zone, > 100 m), and inorganic particles (from the resuspended nepheloid layer). This approach is a useful one for determining the bulk particle composition from observations of the particle backscattering and particle scattering coefficients (in both cases the effect of water are removed, either by correction or by calibration) and to a lesser degree, the power-law slope. Algal cells, and other strongly absorbing particles, exhibit the lowest backscattering ratios (~0.5%) due to their large water content (Aas, 1996), while other weakly-absorbing organic and detrital particles have higher ratios (near 1%) and inorganic particles have the highest ratios (~2%). Boss et al. (2004), however, found that absorption impacts the backscattering coefficient of highly refractive particles more than lesser refractive particles, adding some uncertainty to our ability to invert for the index of refraction of these particles in the wavelengths were they may strongly absorb, e.g. in the blue. Thus for equivalent particle concentration and size, strongly absorbing algal cells will exhibit lower backscattering coefficients than will non-algal particles (organic and inorganic). This is in part what leads to a darkening of the water during algal blooms compared to episodes of sediment resuspension, which brightens the water.

5.5.6 Sensitivity of side or wide angle scattering meters (turbidometers, nephelometers)

Sensors designed to detect side angles or wide angle scattering have been used historically to quantify the suspended particle mass (Table 5.2), although it has been recognized for years that the utility was dependent upon careful calibration with a known scattering suspension or in situ particles (Gibbs, 1974) because of the dependence of the magnitude of the side scattering on, not only particle concentration, but particle composition (real refractive index) and size distribution. An elegant demonstration of the correct calibration procedure was provided by Baker et al. (2001) for the WET Labs LLS. Their application of the technology was to study the suspended particles of the deep sea hydrothermal plumes, which have relatively low suspended loads (< 0.1 $mg.l^{-1}$) but with variable composition and size distributions. Raw voltages from nineteen instruments were intercalibrated using a formazine standard. Clay suspensions of discrete size distributions (Figure 5.21A) were used to quantify the LSS response

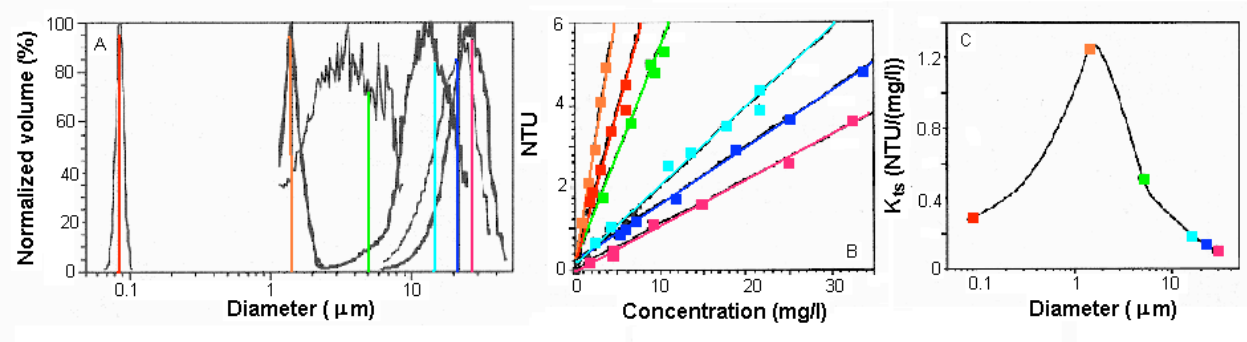

Figure 5.21. An example of the characterization of the WET Labs LSS sensor using dilutions of inorganic clay particles of known size distribution. A. Size distribution of six clay-particle suspensions, determined by Coulter Counter. Vertical lines indicate modal diameter for each suspension. B. LSS response (NTU) to dilutions of the six suspensions, each represented by data points along a line color coded to the size distribution as in part A. The slope of the line is the concentration-specific backscattering coefficient, K_{bs} $(NTU.(mg.l^{-1})^{-1})$. C. Dependence of the concentration-specific backscattering coefficient, K_{bs}, on the mean particle diameter for each suspension, data point color coded as in parts A and B. Modified from Baker et al. (2001). This demonstrates that the LSS is most sensitive to particles in the size range 1 μm and less sensitive to both larger and smaller particles.

as a function of concentration (Figure 5.21B). A different standard curve was observed for each suspension of clay with different PSD. The slope of the standard curve, the concentration-specific backscattering coefficient (called K_{bs} in the original paper, b_b* in the notation of this paper), when plotted as a function of the mean diameter for its respective clay suspension, displayed a Gaussian dependence (Figure 5.21C). Thus the response of the LSS varies

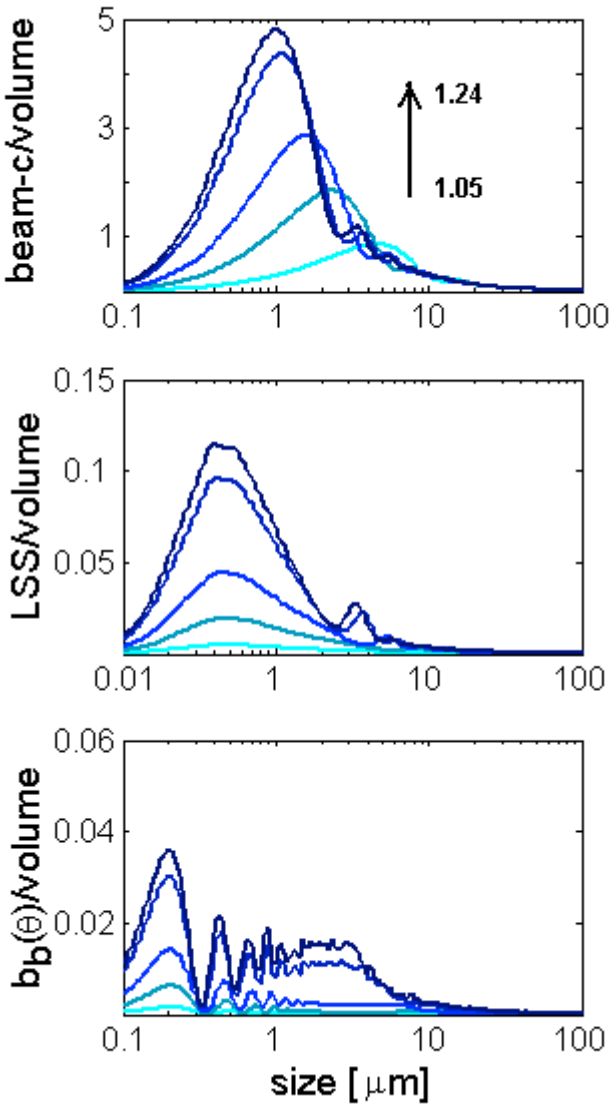

Figure 5.22. Particle volume-specific instrument response as a function of particle diameter for a A. beam transmissometer, B. wide-angle scattering sensor, C. single-angle backscattering sensor, as a function of particle refractive indices (ranging 1.05 to 1.24). As particle refractive index increases, all scattering properties increase. Beam *c* is most sensitive to highly refractive (i.e. mineralic) particles in the range of 1 μm. For less refractive particles (i.e. phytoplankton), beam *c* is most sensitive to particles of diameter 5 μm. Wide angle side scattering is most sensitive to particles in the size range 0.5 μm, regardless of refractive index although the response increases with refractive index. Backscattering is most sensitive to small particles of order 0.2 μm although the relationship is complicated and particles up to 5 μm are effective backscatterers.

significantly with particle size under a constant composition. The utility of this approach is the capability of quantifying the scattering response separately to concentration, composition, and size distribution. However, in-situ, one would need additional IOP measurements to elucidate the cause of a specific change in the signal of a specific IOP (e.g. concentration, composition or size distribution).

5.5.7 What are the Particles Responsible for Scattering in the Ocean?

Having analyzed the IOP response to particle characteristics and the instrument response to IOP variability, it is useful to step back and ask which particles dominate the in situ IOP observations. Here we examine a beam transmissometer (ac-9), a wide angle scattering sensor (LSS), and a single angle backscattering sensor (ECObb). Figure 5.22 shows the theoretical instrumental response as a function of particle size for a range of real refractive indices. This figure is generated by computing the volume scattering function of a population of particles of a specific diameter and integrating that volume scattering function over the theoretical detection angles of each sensor. This is done

for populations of particles of each discrete diameter value. Finally, the instrumental response has been normalized to the total particle volume so that we are looking at the response to a given, or known, particle volume, which is packaged into particles of diameter *D*. Thus, numerous small particles have the same volume of a few large particles. This approach is taken because of the use of scattering sensors to derive volumetric biogeochemical proxies for total suspended solids (TSS) or total particulate organic carbon concentration (POC), neither of which contains size distribution information.

The volume-specific scattering response generally increases with refractive index for all particle sizes, as expected. However, the response of beam *c* to particle size is also a strong function of real refractive index. For beam *c* (Figure 5.22A), the strongest response is for a particle volume composed of 1 μm diameter particles of real refractive index 1.24 (as might be found for some clay suspensions). If the particles have a low real refractive index of 1.05 (typical for phytoplankton), it is the 5 μm diameter particles that yield the strongest mass specific response. Wide angle scattering response (Figure 5.22B) is dominated by the submicron particles of diameter ~ 0.5 μm (which would include microbubbles which have a refractive index of 0.75) with monotonically decreasing response to real refractive index. The particle volume-specific single angle backscattering response (Figure 5.22C) demonstrates a complex dependence on particle diameter. For any given refractive index, it is the small particles of diameter ~ 0.2 μm (clay and virus particles), that yield the strongest response and certainly the particle suspensions characterized by diameters < 3 μm (which would include bacteria and picoplankton) dominate the backscattering signal. These results are consistent with those of Morel and Ahn (1991), Stramski and Kiefer (1991), and Baker et al. (2001) who found, respectively, that (1) the backscattering ratio declines, for monodispersed[8] populations, as particle size increases from 0.1 μm and is lower than that for polydispersed populations, (2) total scattering is dominated by particles in the range 1 μm to 10 μm and (3) backscattering by 0.1 μm to 1 μm particles. Note that Figure 5.22 provides the shape of the relative contribution of each size class to the IOP for a power-law PSD with $\xi = 4$.

In terms of phytoplankton, only the very small picoplankton would be significant contributors to the particle backscattering. Larger phytoplankton are inefficient backscatterers

[8] Monodispersed refers to the population size distribution, dominated by particles within a narrow size range, as in a monospecific algal bloom. In contrast, polydispersed indicates a population comprised of particles with a large size range.

because of their larger size and because of their strong absorption (imaginary refractive indices). However, it is important to note that they become more important backscatterers at wavelengths for which their absorption is minimal (generally the green region of the spectrum) and thus can still have a significant impact, particularly at the high concentrations that would be encountered during some HABs. In addition, non-sphericity is known to increase backscattering compared to what would be estimated for spherical particles, as assumed in our calculations (Bohren and Singham, 1991).

While these simulations yield much information regarding scattering dependence on size and refractive index as well as instrument response, there are relatively few in situ examples for these dependencies. One approach taken with a WET Labs ECOvsf sensor (measures three backscattering angles at a single wavelength) is to measure the backscattering coefficient on a discrete water sample (must be large volume to prevent sidewall contamination), then to sequentially filter the water through smaller and smaller pore sizes, measuring the backscattering coefficient on each sequential suspension. In this way it is possible to separate the total backscattering coefficient into contributions by particles within each size interval. This approach was conducted on water collected over a tidal cycle in the Damariscotta River Estuary, Maine. For this particular experiment the size fraction 3 µm to 10 µm was found to contribute approximately 50% to the total backscattering coefficient (Figure 5.23). These results were

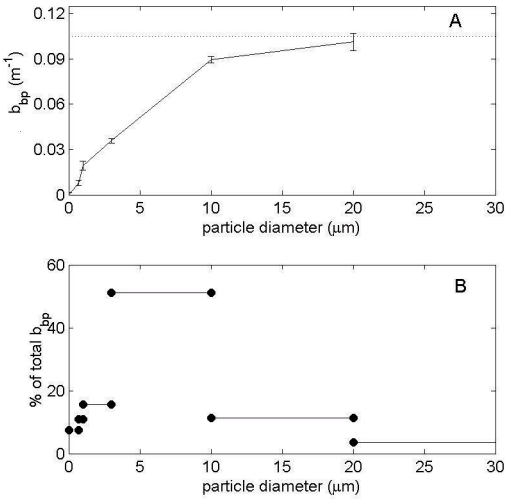

Figure 5.23. Example of the contribution of particles within discrete size ranges to the total particle backscattering for natural waters. A. The cumulative backscattering as a function of particle diameter for discrete size intervals. The total particle backscattering coefficient is indicated by the dotted line (~ 0.105 m^{-1}) and error bars indicate ± 1 standard deviation of >300 realizations. B. The percent contribution to total backscattering by each size interval. A whole water sample collected from the Damariscotta River Estuary was size fractioned (ranges indicated by bars) and the backscattering of each fraction was measured with a WET Labs ECOvsf sensor (440 nm). For this particular sample, which is consistent with other collected during a 24-hour time series experiment, the particles in the 3-10 µm size range dominated the backscattering coefficient. This results in part from their particle-specific backscattering efficiency (which is modeled in Figure 5.22) and their in situ concentration relative to particles in the other size intervals.

consistent throughout the tidal cycle. In keeping with the results of the simulation in Figure 5.22, it confirms that the particles in this size range are efficient backscatterers and were numerous in these waters.

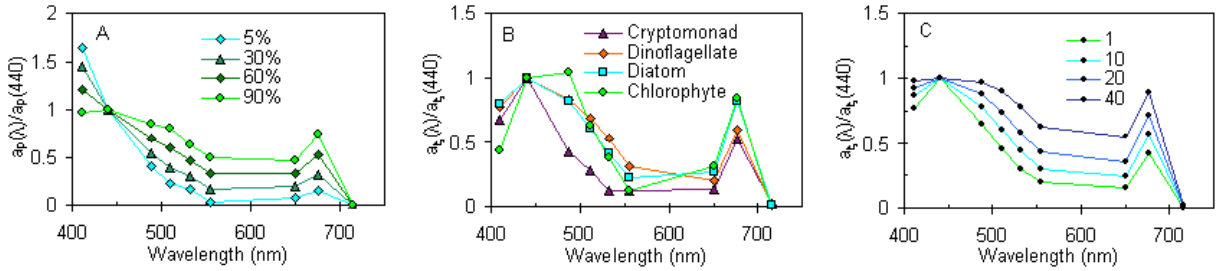

Figure 5.24. Spectral absorption variations associated with phytoplankton properties as would be observed with an ac-9. A. Particulate absorption simulated as a function of percent of algal contribution relative to non-algal particles, scaled to 440 nm. As the contribution by phytoplankton to the total particle absorption decreases, the spectral shape becomes more exponential like that of non-algal particle absorption (see Figure 5.1). B. Spectral phytoplankton absorption for four algal taxa, measured in culture, scaled to 440 nm. The variations in the absorption spectral shapes are caused by variations in pigment composition between the taxa. C. Spectral phytoplankton absorption simulated for a single pigment composition as a function of algal cell diameter (µm), scaled to 440 nm. As the cell size increases, the absorption efficiency at each wavelength decreases, leading to flattened absorption peaks, a process called pigment packaging (Morel and Bricaud, 1981).

5.5.8 What is the IOP measurement response to algal blooms?

The above discussion has centered on the sensitivity of IOP measurements by in situ sensors to weakly absorbing particles (non-pigmented particles with low imaginary refractive indices) in order to aid in the interpretation of in situ IOP observations under typical oceanic conditions. How does the picture change in the presence of intense algal blooms? In this section we investigate how phytoplankton impact the IOPs and provide two specific examples for blooms of *Prorocentrum micans*, a 27-µm diameter dinoflagellate that causes red tides in coastal Gulf of Maine waters and elsewhere, and *Aureococcus anofragefferens*, a 2-µm pelagophyte that causes brown tides in Long Island inlets.

Phytoplankton exhibit a great impact on IOPs because of their spectrally-varying imaginary refractive index, n', which is caused by their specific pigments. These impacts result in variations in both the magnitude and spectral shape of the absorption and scattering spectra. Particle absorption varies spectrally, and the spectral shape changes from the exponentially decaying function of wavelength, typical of non-algal particles, to spectrally complex as the

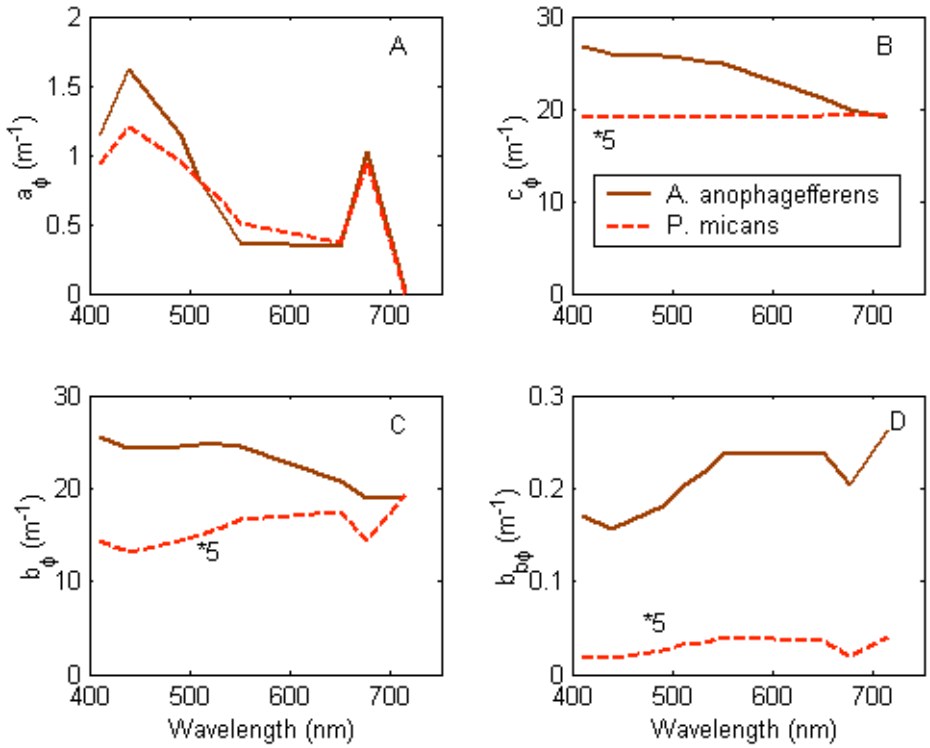

Figure 5.25. Measured inherent optical properties of two algal blooms, *Prorocentrum micans* (red) in the Gulf of Maine and *Aureococcus anophagefferens* (brown) in Long Island Sound. The algae were of sufficient concentrations to turn the water red and brown, respectively. The *a* and *c* coefficients were measured with an ac-9, and used to derive *b*. The measured IOPs and particle size distributions were used to estimate indices of refraction at the ac-9 wavelengths and backscattering was determined using Mie modeling. Note that the *P. micans* values in parts B-D have been multiplied by 5 for ease of resolving spectral shapes.

proportion of phytoplankton cells increases relative to non-algal particles (e.g. Bricaud and Stramski, 1990; Garver et al., 1994; Cleveland, 1995; Sosik et al., 2001; Babin et al., 2003) (Figure 5.24A). Within the phytoplankton component of the particulate matter, the spectral shape changes as pigment ratios vary in response to species composition (e.g. Sathyendranath et al., 1987; Bricaud et al., 1988; Hoepffner and Sathyendranath, 1991; Allali et al., 1997; Bricaud et al., 1998) (Figure 5.24B). Finally, within a single pigment-based algal taxonomic group, the spectral shape of the phytoplankton absorption varies in response to algal cell size and nutrient and light conditions due to packaging of the pigment within the cell (Morel and Bricaud, 1981; Sosik and Mitchell, 1991) (Figure 5.24C).

All of these sources of variability will impact the interpretation of in situ IOP observations during high concentration algal blooms. One of the characteristics of HABs that is

often observed is the dominance of a single species over other species in the community. Here we present two examples of such blooms. The first case is a bloom of *Prorocentrum micans* observed off the Bigelow Laboratory dock in West Boothbay Harbor, ME in 2001 (Etheridge et al., 2002). Chlorophyll concentrations for the bloom of the 27-µm-diameter cell exceeded 100 mg chl.m^{-3}. The observed IOPs for this bloom are shown in Figure 5.25. The absorption shows some flattening of the blue peak due to strong pigment packaging (the specific absorption coefficient at 676 nm was 0.0075 $m^2.mg^{-1}$). The spectral slope of the beam *c* was flat, consistent with dominance by large particles, and the spectral dependence of the scattering and backscattering demonstrate the anomalous dispersion, i.e. depressed scattering, associated with absorption peaks. The backscattering ratio was ~ 0.2% consistent with large, strongly absorbing algal cells.

The bloom resulted in red discoloration of the water (Figure 5.26A and B). This was not because of a specific pigmentation of *P. micans*, but rather the combination of strong absorption in the blue and green wavelengths (400 nm to 550 nm) and spectrally flat backscattering (Figure 5.25A and D). The coastal waters of the Gulf of Maine are characterized by high CDM absorption, originating from the many freshwater inputs. This and the very high *P. micans* absorption in combination with water absorption, resulted in an absorption minimum was shifted to approximately 600 nm to 650 nm, which in combination with the red enhanced backscattering spectrum yielded reflectance maxima in the spectral range 600 nm to 700 nm, or a reddish ocean (Etheridge et al. 2002).

Figure 5.26. Examples of water discoloration during the monospecific HABs in Figure 5.25. A and B. View of coastal waters near Bigelow Laboratory for Ocean Sciences, West Boothbay Harbor Maine, in October 1999, prior to (A) and during (B) the *P. micans* bloom. The water is characteristically green due to high CDM absorption and red during the bloom due to the enhanced blue-green absorption and red backscattering of the *P. micans* cells. (Photos courtesy of M. Keller.) C. Brown water associated with the *Aureococcus anophagefferens* bloom in Quantuck Bay, Long Island, New York in June 2000. Photo courtesy of S. Etheridge.

The second case is that of an *Aureococcus anophagefferens* bloom observed in Quantuck Bay, Long Island, New York in 2000 (Etheridge and Roesler, 2004). In contrast to the IOPs for the large *P. micans* bloom, the IOPs for the 2-µm-diameter *A. anophagefferens* exhibited strongly peaked absorption (chlorophyll specific absorption at 676 nm ~0.2 $m^2.mg^{-1}$), spectrally decreasing beam attenuation and scattering spectra, and backscattering ratios of ~1%, all consistent with strongly absorbing small algal particles. Like the Gulf of Maine, the waters in Long Island Sound are also typically green due to strong CDM absorption. However, the differences between the *A. anophagefferens* absorption compared to that of *P. micans* in the blue/green region of the spectrum (i.e. less green absorption relative to blue) in combination with an order of magnitude increase in the red-enhanced backscattering coefficients are sufficient to change the color of the water to brown, instead of red (Figure 5.26C). Measured radiance reflectance spectra for the brown tide bloom exhibited a broad flat maximum over the range 550 nm to 700 nm compared to the more narrowly peaked spectrum with a maximum of 600 nm observed for *P. micans*.

If we consider a monitoring program that includes IOP observations, how are these two very different blooms resolved by the observations? Against a background of organic particles characterized by a refractive index of 1.05 + i 0.001 and a power-law PSD slope of 4, typical of coastal to oceanic waters, we simulated the development of a bloom by allowing greater proportions of the total particle volume (which was held constant) to be attributed to a superimposed monodispersed algal cells. The phytoplankton were modeled as homogeneous spheres with PSDs described by Gaussian distributions with size ranges of 25 µm ± 15 µm and 2.5 µm ± 1.5 µm, respectively, and with refractive indices of 1.02 + i *n'* (where *n'* was determined from the absorption coefficients in Figure 5.25A and the PSD, Morel and Bricaud, 1981). The VSF for the *P. micans* bloom simulation indicates that as the proportion of the total volume attributed to the large, strongly absorbing algal cells increases, the far forward scattering at angles < 1^o also increases because larger particles diffract light more efficiently than small particles (Figure 5.27A). However, at angles > 1^o, scattering decreases because large absorbing particles are ineffective scatterers (photons entering the particles tend to be absorbed before they are scattered out of the particle). Thus the total scattering, beam attenuation and backscattering coefficients all *decrease* as the proportion of *P. micans* cells increases (Figure 5.27B).

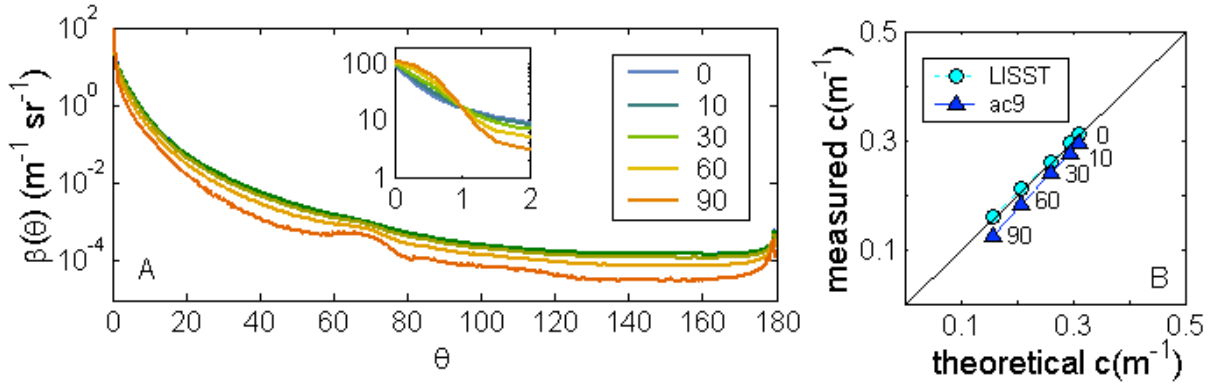

Figure 5.27. A. Volume scattering functions computed for particles with refractive index 1.05 + i 0.001, a Junge slope of 4 with increasing proportions of *P. micans* cells from 0% to 90% of total particle volume. The total particle volume was held constant, only the proportions change. Inset shows the first 2 degrees of resolution. B. The modeled values for beam attenuation coefficient versus the theoretical values for the two instruments as in Figures 14 to 16. As the proportion of *P. micans* increases, beam attenuation coefficients decrease, because phytoplankton are less efficient attenuaters than other weakly absorbing particles.

The scenario is different for the *A. anophagefferens* bloom (Figure 5.28). The VSF exhibits two crossovers as a function of the proportion of algal cells to the total particle volume increases, one at approximately 0.7° and a second at approximately 20°. In this case the diffraction scattering at angles < 0.7° decreases as *A. anophagefferens* increases because these cells are smaller than the average background particles, and thus less efficient diffractors. However, between 0.7° and 20°, the scattering increases with increasing cell proportions. At backscattering angles, the algae are again inefficient backscatterers because of their strong absorption. When the VSF is integrated over all angles it is found that the total scattering and therefore attenuation coefficients increases with increasing proportions of *A. anophagefferens* to the total particle population (Figure 5.28B). However, the backscattering coefficient, as for the case of *P. micans*, decreases as the cell proportion increases, but the backscattering coefficient for *A. anophagefferens* is nearly an order of magnitude greater than that for the same particle volume of *P. micans*, consistent with observations that backscattering is dominated by small particles, even if they are absorbing particles. So for equivalent algal cell volumes, HABs dominated by small cell species will yield brighter waters than those dominated by large cell species if all other components are constant, but generally HABs yield darker waters than those

without high concentrations of algal cells because phytoplankton are less efficient backscatterers than are more weakly absorbing non-algal particles for the same particle volume concentration.

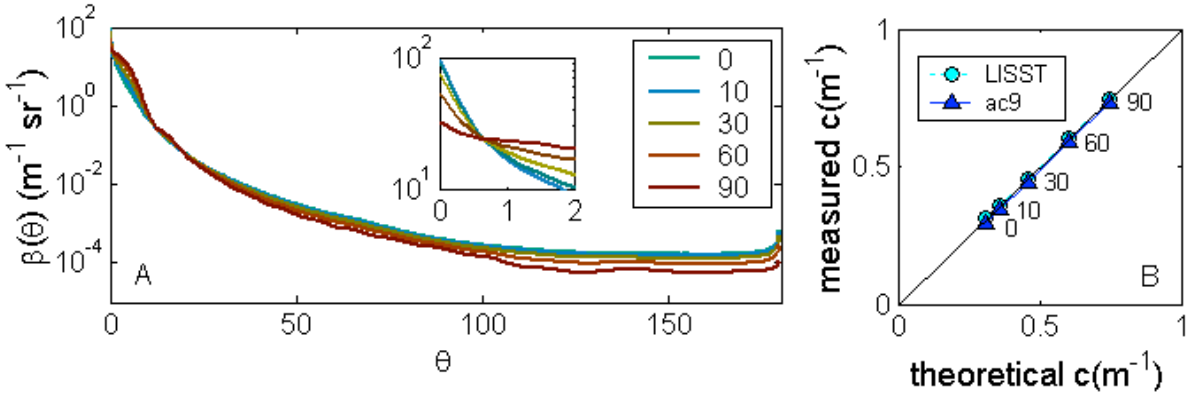

Figure 5.28. A. Volume scattering functions computed for particles with refractive index 1.05 + i 0.001, a Junge slope of 4 with increasing proportions of *Aureococcus anophagefferens* cells from 0% to 90% of total particle volume. The total particle volume has been held constant, only the proportion of *A. anophagefferens* cells relative to background particles changes. Inset shows the first 2 degrees of resolution. B. The modeled values for beam attenuation coefficient versus the theoretical values for the two instruments as in Figure 5.27. As the proportion of *A.. anophagefferens* increases, beam attenuation coefficient increases as the small *A. anophagefferens* cells are more efficient attenuaters than the larger background particles (which might consist of larger cells, aggregates, detrital matter, suspended sediments).

5.6 Employing IOP sensors in a coastal monitoring program

The utility of using in situ observations of IOPs in a coastal monitoring program has been demonstrated above as they can provide information regarding particle concentration and composition, once the instruments are characterized and calibrated to adequate standards. An understanding of the sources of variability in the constituent-specific optical properties, and an understanding of the instrument-specific response to those variabilities are both necessary to interpret in situ observations. While no single IOP model will be applicable to all algal blooms, in situ IOP observations can contribute important information as blooms initiate and develop. These include detection of (1) changes in the proportion of algal absorption to total absorption, (2) changes in the spectral slope of the beam attenuation to indicate bulk particle size changes, (3) changes in the bulk backscattering ratio to indicate changing dominance by algal particles, and (4) changes in near forward VSF indicating changes in the bulk size distribution. The nature of the HAB problem (Chapter 1, Cullen, 2005) will help to dictate which IOPs will be the most

useful. Ancillary measurements of physical and chemical parameters (e.g. temperature, salinity, radiance, turbulence levels, nutrients, pigments) can greatly supplement the IOP measurement to narrow down the likely cause of the change in IOP.

5.6.1 HAB Scenario 1. High algal biomass caused by the target species

For a HAB problem in which any increase in particle attenuation is due to the cells themselves or due to covarying particles, a simple beam transmissometer or scattering sensor might be sufficient for early detection. This is the case for *Aureococcus anophagefferens* in Long Island Sound embayments (Figure 5.29A and B). However, when monitoring such situations

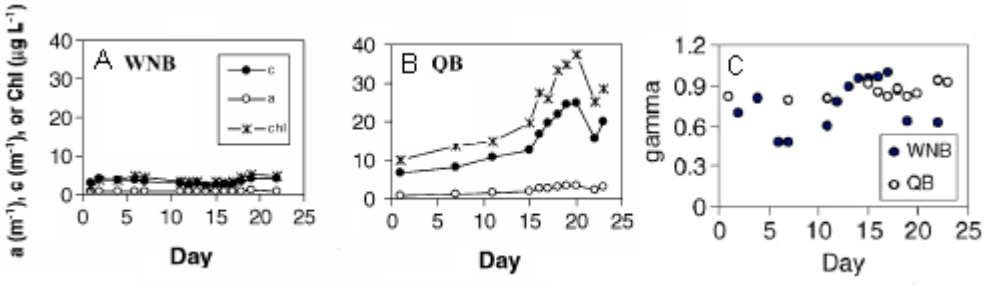

Figure 5.29. Time series of IOP observations during a brown tide bloom, Long Island, NY (Etheridge and Roesler, 2004): beam attenuation, absorption and chlorophyll from West Neck Bay (A) and Quantuck Bay (B), and slope of the particle beam attenuation coefficient (γ) for both sites (C). The phytoplankton community varied in both particle size and pigment composition at WNB although the bulk concentration remained stable. In contrast, a bloom of *Aureococcus anophagefferens* developed at QB as indicated by the increase in the IOP magnitudes and chlorophyll concentration. The indicator of size distribution remained invariant and indicative of small particles, consistent with the *A. anophagefferens* cell size (< 3 µm). These results were verified by microscopy and size fractionated HPLC pigment analyses.

with a full suite of IOP sensors, obtaining more information regarding the ecosystem is possible. This was found for two embayments in Long Island Sound in 2000 (Etheridge and Roesler, 2004). Recurrent brown tide blooms had previously been found in West Neck Bay; for the field program Quantuck Bay was used as the control environment against which the developing brown tide would be viewed. Time series IOP observations were made in two different embayments, one that developed a brown tide and one that did not (Figure 5.29A and B). Estimations of the slope of the particle size distribution derived from the spectral slope of beam *c* indicated that the bay with the *A. anophagefferens* bloom was dominated by smaller particles consistently over the 3-week period while large variations in the estimated particle size slope were observed in the bay

without the brown tide (Figure 5.29C). Size fractionated HPLC pigment analyses and microscopy verified that the non-brown tide phytoplankton community was highly variable in both size and pigment-based taxonomy although the bulk biomass (as estimated by chlorophyll concentration and beam *c*) remained constant, while the brown tide phytoplankton community was dominated by *A. anophagefferens* with virtually no other contributions by other species throughout the bloom. Thus the spectral beam *c* observations contributed significantly to understanding both the biomass aspects of the bloom but also the composition.

5.6.2 HAB Scenario 2. High algal biomass, in which target species just one member of the population

For productive waters with high algal concentrations that are occasionally plagued by blooms of toxic or harmful species, more information than biomass is required. If the targeted species is recurrent and its optical and size properties are known, the spectral IOPs may provide indicators of the target species against the background of the phytoplankton community. In this case, instrumentation to detect particle size distribution and spectral absorption properties may be advantageous. This is the case for *Karenia brevis* off the coast of Florida and *Alexandrium sp.* or *Dinophysis sp.* off the coast of South Africa. Detecting a target species amongst a general population of phytoplankton using the IOPs is likely to depend upon the capability for in situ hyperspectral absorption and algorithms to identify particular features associated with pigment composition (Schofield et al., 1999). This approach has been implemented on the West Florida Shelf using two different in situ technologies: a hyperspectral absorption/attenuation meter (WET Labs HiSTAR; Lohrenz and Schofield, pers. comm.) and a liquid waveguide capillary cell spectrometer (LWCC, essentially a hyperspectral spectrophotometer with ~ 1 nm resolution; Kirkpatrick et al., 2003) in combination with an algorithm called a similarity index (essentially the goodness of fit between the measured absorption spectrum and that associated with the target species). Results suggest that the fraction of chlorophyll associated with *K. brevis* is significantly related to the similarity index derived from LWCC absorption measurements (Kirkpatrick et al., 2000). Recently this spectrometer has been deployed on a glider platform to retrieve three dimensional distributions of *K. brevis* (Schofield et al., 2004).

5.6.3 HAB Scenario 3. Low algal biomass or target species never dominates population

In coastal waters where seasonal algal blooms occur but the target species never reaches high biomass conditions and thus never contributes significantly to the bulk optical properties, IOP observations alone cannot identify the target species of interest. If however, unique behavioral or ecological patterns, such as vertical migration or co-occurrence of target species with other taxa that *are* optically detectable, can result in the development of optical proxies indicating the likely presence of the target species. This is the case with *Alexandrium fundyense* in the Gulf of Maine. For example, in situ observations of spectral or hyperspectral absorption, in combination with optically-based estimates of size distribution, can be used to identify species succession from large diatom communities to dinoflagellates to smaller flagellates, indicating when *Alexandrium sp.* are likely to be found (see section 5.6.4).

5.6.4 Temporal variations in ecosystem structure inferred from in situ IOP observations

An example of the type of time series observations that are available with moored IOP instrumentation is taken from the Gulf of Maine Ocean Observing System (GoMOOS) program. IOP and hydrographic observations of an autumn transition period in the coastal Gulf of Maine waters are shown in Figure 5.30. These observations are from one of ten moorings deployed in the Gulf of Maine, which report real-time hourly observations of meteorologic, hydrographic and optical conditions. In the autumn of 2002, the coastal waters were undergoing destratification, with mixing events occurring the third week of August and the second week of September, separated by restratification, and a final mixing at the beginning of October, which resulted in complete destratification (Figure 5.30A).

Associated with these changes in the thermal structure were significant changes in the optical properties (Figure 5.30B-F). The spectral absorption coefficients, measured with an ac-9 at ~ 3 m, were deconvolved into contributions by the major absorbing constituents (Roesler et al. 1989). The standard deconvolution model, which depends upon an a priori determination of the 440 nm:676 nm ratio for absorption by phytoplankton, was found to converge only if two different ratios were used for the first part and the last part of the time series (1.9 and 1.6, respectively). These yielded two very different spectral shapes for the phytoplankton absorption (Figure 5.30E and F, respectively). Incorporating these two phytoplankton absorption spectral shapes, plus the absorption spectral shapes for NAP and CDM (i.e. Figure 5.1), a linear least squares minimization to the total absorption time series was obtained. The resulting time series

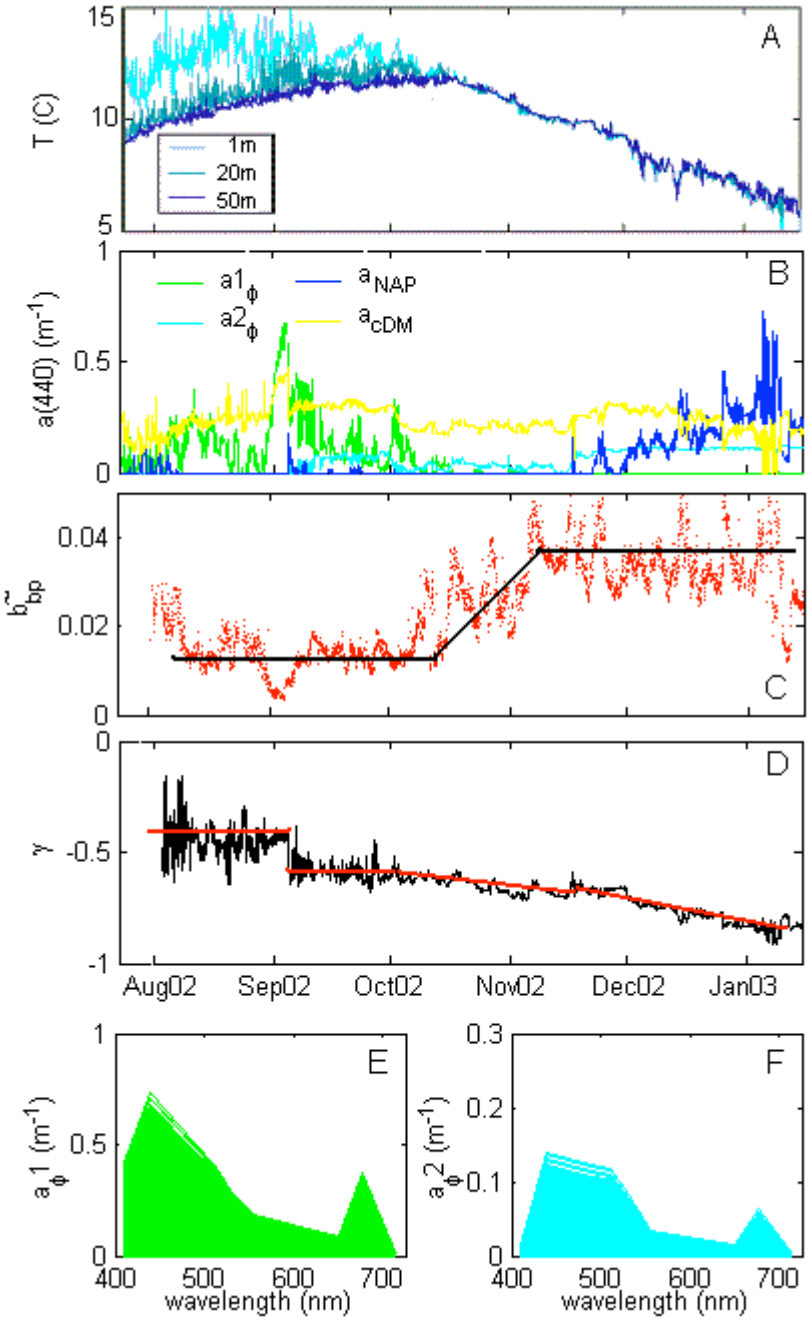

Figure 5.30. Real time hourly observations of temperature, IOPs, and derived optical properties for the period August 2002 to January 2003 from the Eastern Maine Coastal Current, Gulf of Maine (Roesler and Barnard, 2003). A. Temperature at 0 m, 20 m, and 50 m, B. component absorption (440 nm, derived from total measured absorption, see text for details), C. particle backscattering ratio (660 nm), D. spectral slope of particle attenuation, γ, and E and F. spectral shape of two phytoplankton absorption components, the temporal pattern for each shown in part B. See text for details.

of the magnitude of constituent absorption at 440 nm indicates that a_{CDM} is relatively invariant for this time period, while a_{NAP} is negligible until mid-November, when it increases dramatically.

The first component of phytoplankton absorption is associated with the small algal blooms that occur in response to the series of destratification/stratification events until mid-October. Once the water column becomes destratified, and presumably well-mixed, the second phytoplankton component becomes dominant. While there was no in situ validation, the spectral shapes of these two components are consistent with these observations, the first exhibiting strong peaks, characteristic of phytoplankton growing near the surface in a stratified high light environment; the second exhibiting strong pigment packaging characteristic of light limited cells in a deeply mixing water column.

The particle backscattering ratio (Figure 5.30C), which is indicative of particulate composition, is consistent with the particulate composition obtained by absorption inversion. Periods of algal blooms are associated with low backscattering ratios, while the transition from the high concentrations of the high light adapted phytoplankton to lower concentrations of the low light adapted phytoplankton with some contributions by NAP, is associated with backscattering ratios characteristic of more detrital organic particles. Finally, the increase in the NAP absorption component is associated with high backscattering ratio values, consistent with inorganic particles. The spectral slope of the particle attenuation spectrum, γ, is initially ~0.4, indicating larger particle dominance until the decline of the large bloom (Figure 5.30D). The value drops to ~ 0.6 as the proportion of high light adapted cells declines. The slope continues to decrease as the particulate pool changes composition to the low light adapted algal population and finally to the inorganic particle population.

Analysis of residual currents at this mooring (data not shown) indicate that this period of increasing inorganic particles is associated with strong offshore currents. The inshore region is known for deep tidal mixing, which during destratified periods resuspends sediments into the surface layer, which would then be transported offshore past the mooring. The combination of hydrographic and optical observations, complete with analysis of derived optical properties allows the structure of the dissolved and particulate pools (including phytoplankton, other organic and inorganic particles) to be characterized on highly resolved times scales. Such an approach, when applied to a HAB situation can provide information not only on algal absorption properties, but co-occurring particulate and dissolved matter and variations in particle size

distribution. As outlined in the three HAB scenarios above, this may provide direct information on the HAB itself, or ancillary information about the ecosystem as a whole with which to interpret HAB dynamics. While biofouling of optical instrumentation is of great concern in moored situations, great strides have been made in reducing biofouling with copper coatings, tubing and shutters (see chapters 2 and 11; Chang and Dickey, 2005; Lehaitre et al., 2005) Additionally, employing multiple optical sensors to derive redundant optical properties yields a method for in situ validation: phytoplankton concentration via fluorometry and absorption (e.g. by decomposition or the magnitude of the absorption at 676 nm), or particle composition via absorption deconvolution and particle backscattering ratios.

5.7 The State-of-the-art and Future in situ IOP observations

In situ analysis of seawater to further discern particle specific IOPs has lead to some unique observations about the concentration, composition and distribution of algal groups. One type of manipulation is in situ size fractionation, in which filter cartridges are placed at the intake port of the ac-9 (Roesler et al. 1997). By choosing the filter size carefully, the target species in question can be isolated from the bulk particles and the optical properties monitored for changes in concentration. Other manipulations might be chemical, such as acidification of the water sample to dissolve carbonate cell walls (Balch et al. 1999). This approach has been used to detect the presence of coccolithophorids in situ. A third manipulation is pressurization to burst gas vacuoles associated with cyanobacteria such at *Trocodesmium* spp. (Subramanian et al. 1999) to identify their presence in situ.

A promise for the future is the detection of pigment based taxonomic groups based upon hyperspectral absorption observations. While the absorption ratios detected at ac-9 wavelengths are sufficient to resolve major groups (Figure 5.24B), the aim is that with increased spectral resolution, even finer distinctions can be made. This is the basis for the 'breve-buster' discussed in section 5.6.2. The 0.5-m path length Liquid Waveguide Capillary Cell and in situ size fractionation to examine the high resolution absorption properties of *Karenia brevis*-sized particles, which in combination with the similarity index algorithm (Millie et al., 1997), appears to detect the presence of *K. brevis* (Kirkpatrick et al., 2000). This instrumentation package is currently being deployed aboard an AUV, which provide high resolution observations in three dimensions.

Finally, the near future is exploding with the miniaturization of optical sensors. This miniaturization will lead to the incorporation of optical sensors on a range of platforms that have remained illusive due to size, mass and power constraints. These include gliders, drifters, and floats (Rudnick and Perry, 2003; Chapter 12, Griffiths, 2005). Sensor miniaturization is currently being employed in the development of hybrid sensors such as those that detect both fluorescence and backscattering in a can the size of a hockey puck (WET Labs). The explosion of observational platforms and optical instrument development in combination with optical theory will lead to detection of oceanic constituents on time and space scales that are currently only a dream.

5.8 References

Aas, E. (1996). Refractive index of phytoplankton derived from its metabolite composition. *J. Plankton Res*. 18: 2223–2249.

Agrawal, Y.C. and Pottsmith, H.C. (2000). Instruments for Particle Size and Settling Velocity Observations in Sediment Transport. *Mar. Geol*. 168: 89-114.

Allali, K., Bricaud, A., and Claustre, H. (1997). Spatial variations in the chlorophyll-specific absorption coefficients of phytoplankton and photosynthetically active pigments in the Equatorial Pacific. *J. Geophys. Res*. 102: 12413-12423.

Babin, M., Morel, A., Fournier-Sicre, V., Fell, F., and Stramski, D. (2002). Light scattering properties of marine particles in coastal and oceanic waters as related to the particle mass concentration. *Limnol. Oceanogr*. 48: 843-859.

Babin, M., and Stramski, D. (2002). Light absorption by aquatic particles in the near-infrared spectral region. *Limnol. Oceanogr*. 47: 911-915

Babin, M., and Stramski, D. (2005). Variations in the mass-specific absorption coefficient of mineral particles suspended in water. *Limnol. Oceanogr*. In press.

Babin, M., Stramski, D. Ferrari, G.M., Claustre, H., Bricaud, A., Obolensky, G., and Hoepffner, N. (2003). Variations in the light absorption coefficients of phytoplankton, non-algal particles, and dissolved organic matter in coastal waters around Europe. *J. Geophys. Res.* 10.1029/2001JC000882.

Bader, H. (1970). The hyperbolic distribution of particle sizes. *J. Geophys. Res*. 75: 2823- 2830.

Baker, E. T., Tennant, D.A., Feely, R.A., Lebon, G.T., and Walker, S.L. (2001). Field and laboratory studies on the effects of particle size and composition on optical backscattering measurements in hydrothermal plumes. *Deep-Sea Res. I* 48: 593-604.

Balch, W. M., Drapeau, D.T., Cucci, T.L., Vaillancourt, R.D., Kilpatrick, K.A. and Fritz, J.J. (1999). Optical backscattering by calcifying algae-Separating the contribution by particulate inorganic and organic carbon fractions. *J. Geophys. Res.* 104: 1541-1558.

Bohren, C.F. and Huffman, D.R. (1983). *Absorption and Scattering of Light by Small Particles*. Wiley, New York.

Bohren, C.F. and Singham, S.B. (1991). Backscattering by nonspherical particles: A review of methods and suggested new approaches. *J. Geophys. Res*. 96: 5269–5277.

Boss, E. and Pegau, W.S. (2001). Relationship of light scattering at an angle in the backward direction to the backscattering coefficient. *Appl. Opt*. 40: 5503-5507.

Boss, E., Pegau, W.S., Gardner, W.D., Zaneveld, J.R.V., Barnard, A.H., Twardowski, M.S., Chang, G.C., and Dickey, T.D. (2001b). The spectral particulate attenuation and particle size distribution in the bottom boundary layer of a continental shelf. *J. Geophys. Res*. 106: 9509–9516.

Boss, E., Twardowski, M.S., and Herring. S. (2001a). The shape of the beam attenuation spectrum and its relation to the size distribution of oceanic particles. *Appl. Opt*. 40: 4885-4893.

Boss E., Pegau, W.S., Lee, M., Twardowski, M.S., Shybanov, E., Korotaev, G., and Baratange, F. (2004). The particulate backscattering ratio at LEO 15 and its use to study particles composition and distribution. *J. Geophys. Res*., 109, C1, C0101410.1029/2002JC001514.

Bricaud, A., Bedhomme, A-L., and Morel, A. (1988). Optical properties of diverse phytoplankton species: experimental results and theoretical interpretation. *J. Plankton Res.* 10: 851-873.

Bricaud, A., Morel, A., Babin, M., Allali, K., and Claustre, H. (1998). Variations of light absorption by suspended particles with the chlorophyll a concentration in oceanic (Case 1) waters: analysis and implications for bio-optical models. *J. Geophys. Res.* 103: 31033-31044.

Bricaud, A., Morel, A., and Prieur, L. (1981). Absorption by dissolved organic matter of the sea (yellow substance) in the UV and visible domains. *Limnol. Oceanogr*. 26: 43-53.

Bricaud, A., Morel, A., and Prieur, L. (1986). Optical efficiency factor of some phytoplankters. *Limnol. Oceanogr*. 28: 816-832.

Bricaud, A., Roesler, C.S., and Zaneveld, J.R.V. (1995) In situ methods for measuring the inherent optical properties of ocean waters. *Limnol. Oceanogr*. 40: 393-410.

Bricaud, A., and Stramski, D. (1990). Spectral absorption coefficients of living phytoplankton and nonalgal biogenous matter: A comparison between the Peru upwelling area and the Sargasso Sea. *Limnol. Oceanogr*. 35: 562-582.

Bricaud, A., Zaneveld, J.R.V., and Kitchen, J.C. (1992). Backscattering efficiency of coccolithophorids: use of a three-layered sphere model. In: Gilbert, G.D. (ed), *SPIE vol. 1750 Ocean Optics XI*, p. 27-33.

Carder, K.L., Steward, R.G., Harvey, G.R., and Ortner, P.B. (1989). Marine humic and fulvic acids: Their effects on remote sensing of ocean chlorophyll. *Limnol. Oceanogr*. 34: 68-81.

Chang, G.C. and Dickey, T.D. (2005). Interdisciplinary sampling strategies for detection and characterization of harmful algal blooms. In: Babin, M., Roesler, C.S., and Cullen, J.J. (eds.), *Real-time observation systems for ecosystem dynamics and harmful algal blooms*. UNESCO, Paris.

Claustre, H., Fell, F., Oubelkheir, K., Prieur, L., Sciandra, A., Gentili, B., and Babin, M. (2000). Continuous monitoring of surface optical properties across a geostrophic front: biogeochemical inferences. *Limnol. Oceanogr*. 45: 309-321.

Cleveland, J.S. (1995). Regional models for phytoplankton absorption as a function of chlorophyll a concentration. *J. Geophys. Res*. 100: 13333-13344.

Cullen, J.J. (2005). Observation and prediction of harmful algal blooms. In: Babin, M., Roesler, C.S., and Cullen, J.J. (eds.), *Real-time observation systems for ecosystem dynamics and harmful algal blooms*. UNESCO, Paris.

Cullen, J.J. and Lewis, M.R. (1995). Biological processes and optical measurements near the sea surface: Some issues relevant to remote sensing. *Geophys. Res.* 100: 13255-13266.

Cullen, J.J. and Davis, R.F. (2003). The blank can make a big difference in oceanographic measurements. *Limnol. Oceanogr. Bull*. 12: 29-35.

Diehl, P. and Haardt, H. (1980). Measurement of the spectral attenuation to support biological research in a 'plankton tube' experiment. *Oceanologica Acta* 3: 89–96.

Ducha, J. and Kubin, S. (1976). Measurement of in vivo absorption spectra of microscopic algae using bleached cells as a reference sample. *Arch. Hydrobiol. Suppl*. 49: 199-213.

Etheridge, S.M. 2002. *Ecophysiology and Optical Detection of Harmful Algal Blooms*. Ph.D. Dissertation, University of Connecticut, Storrs, 184 pp.

Etheridge, S.M and Roesler, C.S. (2004). Temporal variations in phytoplankton, particulates, and colored dissolved organic material based on optical properties during a Long Island brown tide compared to an adjacent embayment. *Harmful Algae* 3: 331-342.

Etheridge, S.M., Roesler, C.S., Franklin, H.M., and Boss, E. (2002). Do bio-optical parameters and relationships apply to extreme algal blooms? In: Ackleson, S. and Cleveland, J. (eds.), *Proc. Ocean Optics XVI*, Hawaii.

Garver, S.A., Siegel, D.A., and Mitchell, B.G. (1994). Statistical variability of near-surface particulate absorption spectra: What can a satellite ocean color imager see? *Limnol. Oceanogr*. 39: 1349-1367.

Gibbs, R.J. (1974). Principles of studying suspended materials in water. In: Gibbs, R.J. (ed.), *Suspended Solids in Water*. Plenum, New York, p. 3-15.

Gordon, H.R. (1974). Mie theory models of light scattering by ocean particulates. In: Gibbs, R.J. (ed.), *Suspended Solids in Water*. Plenum, New York, p. 73-80.

Gordon, H.R. (1993). Sensitivity of radiative transfer to small-angle scattering in the ocean: Quantitative assessment. *Appl. Opt*. 32: 7505-7511.

Griffiths, G. 2005. Glider and autonomous underwater vehicle observing systems. In: Babin, M., Roesler, C.S., and Cullen, J.J. (eds.), *Real-time observation systems for ecosystem dynamics and harmful algal blooms*. UNESCO, Paris.

Hoepffner, N. and Sathyendranath, S. (1991). Effect of pigment composition on absorption properties of phytoplankton. *Mar. Ecol. Prog. Ser*. 73: 11-23.

Iturriaga, R and Siegel, D.A. (1989). Microphotometric characterization of phytoplankton and detrital absorption properties in the Sargasso Sea. *Limnol. Oceanogr*. 34: 1706-1726.

Kirk, J.T.O. (1992). Monte Carlo modeling of the performance of a reflecting tube absorption meter. *Appl. Opt*. 31: 6463-6468.

Kirk, J.T.O. (1994). *Light and Photosynthesis in Aquatic Ecosystems*. Cambridge University Press, Cambridge.

Kirkpatrick, G., Millie, D., Moline, M. and Schofield, O. (2000). Optical discrimination of a phytoplankton species in natural mixed populations. *Limnol. Oceanogr*. 45: 467-471.

Kirkpatrick, G. J., Orrico, C., Moline, M.A., Oliver, M., and Schofield, O.M. (2003). Continuous hyperspectral absorption measurements of colored dissolved organic material in aquatic systems. *Appl. Opt.* 42: 6564-6568.

Kishino, M., Takahashi, M., Okami, N., and Ichimura, S. (1985). Estimation of the spectral absorption coefficients of phytoplankton in the sea. *Bull. Mar. Sci*. 37: 634-642.

Kitchen, J. and Zaneveld, J.R.V. (1990). On the non-correlation of the vertical structure of light scattering and chlorophyll *a* in Case I waters. *J. Geophys. Res*. 95: 20237-20246.

Kitchen, J.C. and Zaneveld, J. R. V. (1992). A three-layered sphere model of the optical properties of phytoplankton. *Limnol. Oceanogr*. 37:1680-1690.

Lee, M.E. and Lewis, M.R. (2003). A new method for the measurement of the optical volume scattering function in the upper ocean. *J. Atmos. Ocean. Tech*. 20: 563–571.

Lehaitre, M., Delauney, L., and Compère, C. (2005). Biofouling and underwater measurements. In: Babin, M., Roesler, C.S., and Cullen, J.J. (eds.), *Real-time observation systems for ecosystem dynamics and harmful algal blooms*. UNESCO, Paris.

Logan, B.E. (1993). Theoretical analysis of size distributions determined using screens and filters. *Limnol. Oceanogr*. 38: 372-381.

Maffione, R.A. and Dana, D.R. (1997). Instruments and methods for measuring the backward-scattering coefficient of ocean waters. *Appl. Opt*. 36: 6057-6067.

Mie, G. (1908). Beiträge zur Optik trüber Medien, speziell kolloidaler Metallösungen. *Ann. Physik* 4: 377-455.

Millie, D., Schofield, O.M., Kirkpatrick, G.J., Johnsen, G., Tester, P.A., and Vinyard, B.T. (1997). Detection of harmful algal blooms using photopigments and absorption signatures: A case study of the Florida red tide, *Gymnodinium breve*. Limnol. Oceanogr. 42: 1240–1251.

Moore, C., Zaneveld, J.R.V., and Kitchen, J.C. (1992). Preliminary results from an in situ spectral absorption meter. *Ocean Optics XI, SPIE* 1750: 330-337.

Morel, A. (1973). Diffusion de la lumiere par les eaux de mer. Resultat experimentaux et approch theorique. In : *AGARD Lecture. Series.* NATO, London, pp. 3.1.1.-3.1.76.

Morel, A. (1974). Optical properties of pure water and pure seawater. In: Jerlov, N.G. and Nielsen, E.S. (eds.), *Optical Aspects of Oceanography.* Academic, London, p. 1-24.

Morel, A. (2005). Introduction to optical properties in the sea: Theoretical aspects. In: Babin, M., Roesler, C.S., and Cullen, J.J. (eds.), *Real-time observation systems for ecosystem dynamics and harmful algal blooms*. UNESCO, Paris.

Morel, A. and Ahn, Y.-H. (1990). Optical efficiency factors of free living marine bacteria: Influence of bacterioplankton upon the optical properties and particulate organic carbon in oceanic waters. *J. Mar. Res*. 48: 145-175.

Morel, A. and Ahn, Y.-H. (1991). Optics of heterotrophic nanoflagellates and ciliates: A tentative assessment of their scattering role in oceanic waters compared to those of bacterial and algal cells. *J. Mar. Res*. 49: 177-202.

Morel, A. and Bricaud, A. (1981). Theoretical results concerning light absorption in a discrete medium, and application to specific absorption by phytoplankton. *Deep-Sea Res*. 28A: 1375-1393.

Mueller J.L., Fagion, G.S., McClain, C.R., Pegau, W.S., Zaneveld, J.R.V., Mitchell, B.G., Kahru, M., Wieland, J., and Stramska, M. (2003). Ocean optics protocols for satellite ocean color sensor validation. In: *Inherent Optical Properties: Instruments, Characterizations, Field Measurements and Data Analysis Protocols* NASA/TM-2003-211621/Rev4-Vol.IV.

Musser J., Fry, E., Gray, D., Kattawar, G., Lu, Z., and Xianzhen, Z.X. (2004). Direct measurement of the integrated scattering coefficient b. *Proc. Ocean Optics XVII*, Freemantle.

Oishi, T. (1990). Significant relationship between the backward scattering coefficient of sea water and the scatterance at 120^{o}. *Appl. Opt*. 29: 4658-4665.

Pegau, W.S., Gray, D., and Zaneveld, J.R.V. (1997). Absorption and attenuation of visible and near-infrared light in water: dependence on temperature and salinity. *Appl. Opt*. 36: 6035-6046.

Pegau, W.S. and Zaneveld, J.R.V. (1993). Temperature-dependent absorption of water in the red and near-infrared portions of the spectrum. *Limnol. Oceanogr*. 38: 188-192.

Pegau, W.S., Zaneveld, J.R.V., and Voss, K.J. (1995). Towards closure of the inherent optical properties of natural waters. *J. Geophys. Res*. 100(C7): 13193-13199.

Petzold, T.J. (1972). *Volume Scattering Functions for Selected Ocean Waters*. SIO Ref. 72-78, 79 pp., Scripps Inst. of Oceanogr., La Jolla, Calif.

Roesler, C.S. (1998). Theoretical and experimental approaches to improve the accuracy of particulate absorption coefficients derived from the quantitative filter technique. *Limnol. Oceanogr.* 43: 1649-1660.

Roesler, C.S. and Barnard, A.H. (2003). Temporal variability in ecosystem structure in the Eastern Maine Coastal Current as observed by the Gulf of Maine Ocean Observing System (GOMOOS). *ASLO Aquatic Science Meeting*. Salt Lake City, UT.

Roesler, C. S. and Perry, M.J. (1995). *In situ* phytoplankton absorption, fluorescence emission, and particulate backscattering spectra determined from reflectance. *J. Geophys. Res*. 100(C7): 13279-13294.

Roesler, C.S., Perry, M.J., and Carder, K.L. (1989). Modeling *in situ* phytoplankton absorption from total absorption spectra. *Limnol. Oceanogr*. 34: 1512-1525.

Roesler, C.S., Simeon, J., and Talbot, M.C. (1997). Variability in vertical distributions of size-fractioned component absorption and scattering coefficients in shallow continental shelf waters. *ASLO/AGU Ocean Sciences*, Santa Fe, NM.

Rudnick, D.L. and M.J. Perry, (eds.) (2003). *ALPS: Autonomous and Lagrangian Platforms and Sensors.* Workshop Report, 64 pp., www.geo-prose.com/ALPS.

Sathyendranath, S., Lazarra, L., and Prieur, L. (1987). Variations in the spectral values of specific absorption of phytoplankton. *Limnol. Oceanogr*. 32: 403-415.

Schofield, O., Bosch, J., Glenn, S., Kirkpatrick, G., Kerfoot, J., Moline, M., Oliver, M., and Bissett, P. (2005). Harmful algal blooms in a dynamic environment: How can optics help the field-going and sample-poor biologist? In: Babin, M., Roesler, C.S., and Cullen, J.J. (eds.), *Real-time observation systems for ecosystem dynamics and harmful algal blooms*. UNESCO, Paris.

Schofield, O., Gryzmski, J., Bissett, W.P., Kirkpatrick, G., Millie, D.F., Moline, M.A., and Roesler, C. (1999). Optical monitoring and forecasting systems for harmful algal blooms: Possibility or pipedream? *J. Phycol*. 35: 125-145.

Schofield, O., Glenn, S., Kirkpatrick, G., Jones, C., and Twardowski, M. (2004). Measuring mesoscale in situ optics of the continental shelves with autonomous Webb gliders. *Proc. Ocean Optics XVII*, Freemantle.

Simeon, J., Roesler, C.S., Pegau, W.S., and Dupouy, C. (2003). Sources of spatial variability in light absorbing components along an equatorial transect from 165°E to 150°W. *J. Geophys. Res.* 108(C10): 3333, doi:10.1029/2002JC001613.

Sosik, H.M. 2005. Characterizing seawater constituents from optical properties. In: Babin, M., Roesler, C.S., and Cullen, J.J. (eds.), *Real-time observation systems for ecosystem dynamics and harmful algal blooms*. UNESCO, Paris.

Sosik, H.M., Green, R.E., Pegau, W.S., and Roesler, C.S. (2001). *J. Geophys. Res*. 106: 9455-9472.

Sosik, H.M. and Mitchell, B.G. (1991). Absorption, fluorescence and quantum yield for growth in nitrogen-limited *Dunaliella tertiolecta*. *Limnol. Oceanogr*. 36: 910-921.

Sosik, H.M, Olson, R.J., Neubert, M.G., Shalapyonok, A., and Solow, A.R. (2003). Growth rates of coastal phytoplankton from time-series measurements with a submersible flow cytometer. *ASLO Aquatic Sciences Meeting*, Salt Lake City, UT.

Stramski, D. (1999). Refractive index of planktonic cells as a measure of intracellular carbon and chlorophyll a content. *Deep-Sea Res*. 46: 335-351.

Stramski, D., Bricaud, A., and Morel, A. (2001). Modeling the inherent optical properties of the ocean based on the detailed composition of the planktonic community. *Appl. Opt*. 40: 2929-2945.

Stramski, D. and Kiefer, D.A. (1991). Light scattering by microorganisms in the open ocean. *Prog. Oceanogr*. 28: 343-383.

Stramski, D. and Mobley, C.D. (1997). Effects of microbial particles on oceanic optics: a database of single-particle optical properties. *Limnol. Oceanogr*. 42: 538-549.

Stramski, D., Sciandra, A., and Claustre, H. (2002). Effects of temperature, nitrogen, and light limitation on the optical properties of the marine diatom *Thalassiosira pseudonana*. *Limnol. Oceanogr.*, 47: 392-403.

Stramski, D., Shalapyonok, A., and Reynolds, R.A. (1995). Optical characterization of the oceanic unicellular cyanobacterium *Synechococcus* grown under a day-night cycle in natural irradiance. *J. Geophys. Res*. 100(C7): 13295-13307.

Stramski, D., Boss, E., Bogucki, D., and Voss, K.J. (2004). The role of seawater constituents in light backscattering in the ocean. *Prog. Oceanogr.* 61(1): 27-55.

Subramaniam, A., Carpenter, E.J., and Falkowski, P.G. (1999). Bio-optical properties of the marine diazotrophic cyanobacteria *Trichodesmium* spp. II. A reflectance model for remote-sensing. *Limnol . Oceanogr*. 44: 618-627.

Twardowski, M.S., Sullivan, J.M., Donaghay, P.L., and Zaneveld, J.R.V. (1999). Microscale quantification of the absorption by dissolved and particulate material in coastal waters with an ac-9. *J. Atmos. Ocean. Tech*., 16: 691-707.

Twardowski, M.S., Boss, E., MacDonald, J.B., Pegau, W.S., Barnard, A.H. and Zaneveld, J.R.V. (2001). A model for estimating bulk refractive index from the optical backscattering ratio and the implications for understanding particle composition in Case I and Case II waters. *J. Geophys. Res*. 106: 14129-14142.

Twardowski, M.S., Boss, E., Sullivan, J.M., and Donaghay, P.L. (2004). Reanalysis of the use of an exponential model to describe the spectral shape of absorption by chromophoric dissolved organic matter (CDOM). *Mar. Chem*. 89: 69-88.

Tyler, J.E., Austin, R.W. and Petzold, T.J. (1974). Beam transmissometers for oceanographic measurements, pp. 51-60. In: Gibb, R.J. (ed.), *Suspended Solids in Water*. Plenum, New York.

Ulloa O., Sathyendranath, S. and Platt, T. (1994). Effect of the particle-size distribution on the backscattering ratio in seawater. *Appl. Opt.* 33: 7070-7077.

van de Hulst, H.C. (1957). *Light Scattering by Small Particles*. Wiley, New York.

Volz, F. (1954). Die optik and meterologie der atmospharischen trubung. *Ber. Dtsch. Wetterdienstes* 2: 3047.

Voss, K.J. 1992. A spectral model of the beam attenuation coefficient in the ocean and coastal areas. *Limnol. Oceanogr*. 37: 501-509.

Voss, K.J. and Austin, R.W. (1993). Beam-attenuation measurement error due to small-angle scattering acceptance. *J. Atmos. Oceanic Tech*. 10: 113-121.

Werdell, P.J. and Roesler, C.S. (2003). Remote assessment of benthic substrate composition in shallow waters using multispectral reflectance. *Limnol. Oceanogr*. 48: 557-567.

Zaneveld, J.R.V., Bartz, R., and Kitchen, J.C. (1990). A reflective-tube absorption meter. *Proc. SPIE Int. Soc. Opt. Eng.* 1302: 124-136.

Zaneveld, J.R.V. and Kitchen, J.C. (1995). The variation in the inherent optical properties of phytoplankton near an absorption peak as determined by various models of cell structure. *J. Geophys. Res.* 100: 13309-13320.

Zaneveld, J.R.V., Kitchen, J.C., and Moore, C.C. (1994). Scattering error correction of reflecting -tube absorption meters. *Ocean Optics XII, SPIE* 2258: 44-55.

Zaneveld, J.R.V., Spinrad, R.W., and Bartz, R. (1980). Optical properties of turbidity standards. *Ocean Optics VI, SPIE* 208: 159-168.

Zhang, X., Lewis, M.R., and Johnson, B. (1998). The role of bubbles in the scattering of light in the ocean. *Appl. Opt.* 37: 6525-6536.

Notation

Symbol	Unit	Definition
A	dimensionless	absorptance, the fraction of incident radiant power that is absorbed
a	m^{-1}	absorption coefficient
a*	$m^2.mg^{-1}$	concentration-specific absorption coefficient, for example, a^*_φ, the chlorophyll-specific phytoplankton absorption coefficient has units of $m^2.(mg\ chl)^{-1}$
a_w, a_p, a_φ, a_{CDM}, a_{NAP}, a_{NAOP}, a_{NAIP}	m^{-1}	absorption coefficients for water, particles, phytoplankton, CDM, NAP, NAOP, NAIP, respectively
B	dimensionless	scatterance, the fraction of incident radiant power that is scattered
b	m^{-1}	scattering coefficient
b*	$m^2.mg^{-1}$	concentration-specific scattering coefficient, for example, b^*_{NAOP}, might be expressed as the particulate organic carbon-specific scattering coefficient, with units of $m^2.(mg\ C)^{-1}$
b_f, b_b	m^{-1}	forward and backscattering coefficients, respectively
C	dimensionless	attenuance, the fraction of incident radiant power that is absorbed or scattered
c	m^{-1}	beam attenuation coefficient
c_p	m^{-1}	particle beam attenuation coefficient
CDOM		Chromophoric (or Colored) Dissolved Material, operationally defined by nominal pore size, generally 0.2 μm to 0.7 μm
NAIP		Non-algal inorganic particles, including mineralic sands, clays and biogenic silica and carbonate
NAOP		Non-algal organic particles, including bacteria, zooplankton, detritus
NAP		Non-algal particles, NAOP + NAIP, operationally defined as the particulate material left on a filter after extraction of algal pigments
D	μm	particle diameter
n, n'		real and imaginary indices of refraction relative to water
N	$particles.ml^{-1}$	particle concentration
r	m	distance
T	dimensionless	transmittance, the fraction of incident radiant power that is transmitted
β	$m^{-1}sr^{-1}$	volume scattering function
γ	dimensionless	slope of the power function fit to spectral particle

		beam attenuation coefficient
λ	nm	wavelength
θ	degree	zenith angle
φ	degree	azimuth angle
Φ, Φ_o, Φ_r, Φ_a, Φ_b, Φ_t	mol photon.s^{-1} or Watts	radiant flux, with subscripts o, r, a, b, t indicating incident, at distance r, absorbed, scattered, transmitted, respectively
ξ	dimensionless	slope of the power function fit to particle size distribution, also called Junge slope

Table 5.1. Configuration specifications for commercially available beam attenuation meters.

Instrument	beam source	beam width	acceptance angle (degrees)	path length (cm)
AlphaTracka transmissometer	LED[1]	15 mm	0.86	5
SeaTech transmissometer	collimated incandescent bulb	7 mm	1.5	25
Sequoia LISST	solid state diode laser	6 mm	0.018, 0.036	5, 10
WET Labs ac9	collimated incandescent bulb	10 mm	0.7	25
WET Labs cstar	LED	10 mm	1.5, 1.9	25, 10

[1]light emitting diode

Table 5.2. Instrumental configuration of commercially available turbidity and scattering sensors. All beams are divergent (see Figure 5.8), but differ in whether they have a narrow (< 45^o) or wide (> 45^o) solid angle.

Instrument name	beam width	Detector acceptance angle(s) and FOV	Wavelength (nm), λ
D&A Tech OBS	narrow	140^o to 160^o	875 (LED)
HOBILabs Hydroscat	narrow	$140^o \pm 10°$	2 or 6 selectable filters
SeaPoint turbidometers	wide	15^o to 150^o	880 (LED)
WET Labs NTU	narrow	$140^o \pm 10°$	700 (LED)
WET Labs LSS	wide	45^o to 145^o	880 (LED)
WET Labs ECObb	narrow	$117^o \pm 10°$	470, 528, 660, 800 (LED)
WET Labs ECOvsf	narrow	110^o, 125^o, 150^o ±10°	470, 528, 660, 800 (LED)

Figure Captions

Figure 5.1. Characteristic absorption spectra for bulk seawater constituents normalized to the mean absorption: water (dark blue), phytoplankton (green), colored dissolved matter (dash orange), non-algal particulate organic matter (solid cyan), non-algal particulate inorganic matter (dotted black).

Figure 5.2. Characteristic scattering spectra for major constituents normalized to the mean scattering: water (dotted dark blue), large and small phytoplankton (solid green and dashed dark green, respectively), and large and small weakly absorbing particles (solid cyan and dashed blue, respectively.

Figure 5.3. Diagram of the scattering angles, θ, where the bold arrow at left signifies the incident beam, forward scattering is indicated by the solid arrow and angle θ_f, and backscattering by the dashed arrow and angle θ_b. Forward scattering occurs in the forward white hemisphere ($\theta = 0$ to $\pi/2$) while backscattering occurs in the backward shaded hemisphere ($\theta = \pi/2$ to π) and azimuthal symmetry is assumed. In a bulk sense, the symmetry assumption holds in the ocean because, although particles are neither spherical nor homogeneous, they are randomly oriented.

Figure 5.4. Conceptual diagram of radiant flux through an infinitesimal layer of thickness Δr. Energy is conserved such that the incident flux is either scattered by the layer (red), absorbed by material in the layer (blue), or transmitted through the layer unattenuated (black).

Figure 5.5. Volume scattering functions (VSFs) observed for natural waters from three optically-diverse environments: clear open ocean Bahamas, coastal Catalina Channel, and turbid San Diego Harbor (data from Petzold, 1972). Inset shows the VSFs for the first degree of forward scattering on a linear scale. Beam transmissometers have finite acceptance angles that capture this far forward scattered light and attribute it to unattenuated flux.

Figure 5.6. Conceptual diagram of the radiant flux in a beam transmissometer in which incident flux, Φ_o is multiply scattered (red arrows, Φ_B) or transmitted (white arrows, Φ_T) into the detector. In this case the geometric path length, r, is smaller than the optical path length for some photons, described by the sum of the red arrows.

Figure 5.7. Conceptual diagram of the radiant flux in a reflecting tube absorption meter in which incident flux is absorbed, transmitted, scattered into the detector, reflected off the side walls into the detector, scattered out of the cuvette, or multiply scattered.

Figure 5.8. Conceptual diagram of a single angle backscattering sensor. The incident irradiance, Φ_o, is a divergent beam with a known solid angle (bold arrow), the detector, likewise has a known detection solid angle. The detected scattered flux, Φ_B (bold red arrow), occurs about the central backscattering angle, θ, within a volume (cyan) defined by the intersection of the incident and detected solid angles. The geometric path length is defined by the sum of the geometric lengths of the bold arrows. Simplified from Maffione and Dana (1997).

Figure 5.9. A. Relationship between the normalized volume backscattering function and backscattering angle for a range of volume scattering functions from pure water to Petzold's San Diego Harbor (see Figure 5.5) (from Boss and Pegau, 2001). The angle at which they intersect is ~ 117°. B. Graphical representation of the calculation of the backscattering coefficient from three point observations at discrete angles as in eqn. (5), the integration of the product of the volume scattering function, β, and the sin of the scattering angle, θ, shown here for a typical oceanic VSF (black). Observational detection angles of the WET Labs VSF meter (black symbols), and the data point at 180° (cyan symbol), which is necessarily zero because $\sin(180^o) = 0$. A third order polynomial fit to the four data points (red) is used in the integration over θ to determine the backscattering coefficient.

Figure 5.10. Hypothetical time course in pure water IOP observations relative to pre-deployment factory calibration. An observed linear trend between pre- (filled square) and post- (filled diamond) deployment factory calibration is given by circles, a step function is given by triangles. These daily observations would indicate how to apply factory calibrations to deployment observations during post-processing: a linear interpolation between the pre- and post deployment calibrations or the pre-deployment calibration until day 11 and the post-deployment calibration from day 12 through day 15.

Figure 5.11. Example of observed attenuation and absorption measured with an ac-9 in stratified coastal waters. Depth profiles of raw attenuation (A) and absorption (B) observations using a pre-deployment factory calibration at 9 wavelengths. Attenuation and absorption spectra (C and D, respectively) taken from discrete depths within and below the mixed later and at the 2 m absorption peak. Spectra corrected for post-deployment calibrations shown in black lines.

Figure 5.12 A. Absorption spectrum from the deep layer, as in Figure 5.11D, before and after temperature and salinity correction (blue square and black triangles, respectively). B. The absorption spectrum from the absorption peak in Figure 5.11D, after applying post-calibrations and temperature and salinity corrections, corrected for scattering by three different models. See text for details.

Figure 5.13. A. Size distribution for oceanic particles. Solid line represents a Junge slope of 4. Particle concentration units are differential with respect to size interval. From Stramski and Kiefer (1989). B. Range of particle size distributions as in A, for Junge slopes ranging from 3 to 5 used in simulations in the following figures.

Figure 5.14. A. Volume scattering functions for a range of particle concentrations (1 to 50 arbitrary units) for particles obeying a Junge distribution with slope of 4 and a refractive index of 1.05 + i 0.001. B. Modeled values for beam attenuation coefficient coefficients for the samples in part A that would result from measurements made with a LISST and an ac-9 versus the theoretical beam attenuation coefficients, given their detection angle responses.

Figure 5.15. A. Volume scattering functions for particles with a range of real refractive index, obeying a Junge distribution with a slope of 4 and with an imaginary refractive index of 0.001. Curves have been normalized to total particle volume to remove the effects of biomass. Inset shows the first 2° of resolution on a linear scale. B. The beam attenuation coefficients for the

samples in part A that would result from measurements made with the two instruments versus the theoretical values, as in Figure 5.14.

Figure 5.16. A. Volume scattering functions for particles obeying the Junge distribution with a range of slopes and with a refractive index of 1.05 + i 0.001. Curves have been normalized to total particle volume to remove the effects of biomass. Inset shows the first degree of resolution on a linear scale. Note the VSF crossover occurs in the far forward scattering, with the Junge slope of 3 (dominance by larger particles) exhibiting the strongest scattering at the smallest angles and the Junge slope of 5 (dominance by smaller particles) the strongest side and backscattering. B. The beam attenuation coefficients for the samples in part A that would result from measurements made with the two instruments versus the theoretical values, as in Figure 5.14. The values of the Junge slope are indicated, showing the hysteresis. The maximal value of beam c occurs at a Junge slope of 4.

Figure 5.17. Conceptual diagrams of the Sequoia LISST, which measures the VSF in the far forward direction at 32 angular intervals. A. A laser passes through a lens into the sample compartment, called the scattering volume. B. Scattering events within the scattering volume cause photos to pass through a lens such that all scattering events along the optical path at angle θ are focused onto the detector at the same radial distance from the center of the detector, regardless of where in the sample chamber they occur. C. The detector consists of 32 concentric ring detectors arranged in quarter circle arcs, each a defined radial distance from the center and thus each associated with a unique forward scattering angle, θ. Illustrations from the LISST manual.

Figure 5.18. Configuration of the HOBI Labs Hydroscat 6. A. Top view of the sensor head showing 6 source/detector pairs. Source locations are shaded. Arrows indicate the associated detector location for each source. B. Side view of instrument showing the cross section of one source beam and detection field of view (arrows); associated backscattering sampling volume is in gray. Illustrations from the Hydroscat manual.

Figure 5.19. Conceptual diagram of the sensor head (left) and cross section (right) of the WET Labs ECOvsf showing the three light emitting diodes (red) and the single detector (black). The three LEDs emit light at three difference angles relative to the sensor head and relative to the single detector leading to detection of backscattering centered at 110^o, 125^o, and 150^o, from top to bottom, respectively. Illustrations from the ECOvsf manual.

Figure 5.20. Theoretical relationship between the particle backscattering ratio and the Junge slope of particle size distribution with lines of constant real refractive index varying from 1.02 to 1.20. Superimposed are data clusters for in situ observations of particle backscattering ratio and the Junge slope (determined from c_p observations and eqns. 14 and 15), taken from the subsurface chlorophyll maximum (green), deep water column (cyan), and benthic nepheloid layer (brown). The three data clusters are dominated by algal particles, non-algal organic particles, and mineral particles, with backscattering ratios of approximately 0.005, 0.0125, 0.02, respectively. Modified from Twardowski et al. (2001).

Figure 5.21. An example of the characterization of the WET Labs LSS sensor using dilutions of inorganic clay particles of known size distribution. A. Size distribution of six clay-particle suspensions, determined by Coulter Counter. Vertical lines indicate modal diameter for each suspension. B. LSS response (NTU) to dilutions of the six suspensions, each represented by data points along a line color coded to the size distribution as in part A. The slope of the line is the concentration-specific backscattering coefficient, K_{bs} (NTU.(mg.l^{-1})$^{-1}$). C. Dependence of the concentration-specific backscattering coefficient, K_{bs}, on the mean particle diameter for each suspension, data point color coded as in parts A and B. Modified from Baker et al. (2001). This demonstrates that the LSS is most sensitive to particles in the size range 1 μm and less sensitive to both larger and smaller particles.

Figure 5.22. Particle volume-specific instrument response as a function of particle diameter for a A. beam transmissometer, B. wide-angle scattering sensor, C. single-angle backscattering sensor, as a function of particle refractive indices (ranging 1.05 to 1.24). As particle refractive index increases, all scattering properties increase. Beam *c* is most sensitive to highly refractive (i.e. mineralic) particles in the range of 1 μm. For less refractive particles (i.e. phytoplankton), beam *c* is most sensitive to particles of diameter 5 μm. Wide angle side scattering is most sensitive to particles in the size range 0.5 μm, regardless of refractive index although the response increases with refractive index. Backscattering is most sensitive to small particles of order 0.2 μm although the relationship is complicated and particles up to 5 μm are effective backscatterers.

Figure 5.23. Example of the contribution of particles within discrete size ranges to the total particle backscattering for natural waters. A. The cumulative backscattering as a function of particle diameter for discrete size intervals. The total particle backscattering coefficient is indicated by the dotted line (~ 0.105 m^{-1}) and error bars indicate ± 1 standard deviation of >300 realizations. B. The percent contribution to total backscattering by each size interval. A whole water sample collected from the Damariscotta River Estuary was size fractioned (ranges indicated by bars) and the backscattering of each fraction was measured with a WET Labs ECOvsf sensor (440 nm). For this particular sample, which is consistent with other collected during a 24-hour time series experiment, the particles in the 3-10 μm size range dominated the backscattering coefficient. This results in part from their particle-specific backscattering efficiency (which is modeled in Figure 5.22) and their in situ concentration relative to particles in the other size intervals.

Figure 5.24. Spectral absorption variations associated with phytoplankton properties as would be observed with an ac-9. A. Particulate absorption simulated as a function of percent of algal contribution relative to non-algal particles, scaled to 440 nm. As the contribution by phytoplankton to the total particle absorption decreases, the spectral shape becomes more exponential like that of non-algal particle absorption (see Figure 5.1). B. Spectral phytoplankton absorption for four algal taxa, measured in culture, scaled to 440 nm. The variations in the absorption spectral shapes are caused by variations in pigment composition between the taxa. C. Spectral phytoplankton absorption simulated for a single pigment composition as a function of algal cell diameter (μm), scaled to 440 nm. As the cell size increases, the absorption efficiency at each wavelength decreases, leading to flattened absorption peaks, a process called pigment packaging (Morel and Bricaud, 1981).

Figure 5.25. Measured inherent optical properties of two algal blooms, *Prorocentrum micans* (red) in the Gulf of Maine and *Aureococcus anophagefferens* (brown) in Long Island Sound. The algae were of sufficient concentrations to turn the water red and brown, respectively. The *a* and *c* coefficients were measured with an ac-9, and used to derive *b*. The measured IOPs and particle size distributions were used to estimate indices of refraction at the ac-9 wavelengths and backscattering was determined using Mie modeling. Note that the *P. micans* values in parts B-D have been multiplied by 5 for ease of resolving spectral shapes.

Figure 5.26. Examples of water discoloration during the monospecific HABs in Figure 5.25. A and B. View of coastal waters near Bigelow Laboratory for Ocean Sciences, West Boothbay Harbor Maine, in October 1999, prior to (A) and during (B) the *P. micans* bloom. The water is characteristically green due to high CDM absorption and red during the bloom due to the enhanced blue-green absorption and red backscattering of the *P. micans* cells. (Photos courtesy of M. Keller.) C. Brown water associated with the *Aureococcus anophagefferens* bloom in Quantuck Bay, Long Island, New York in June 2000. Photo courtesy of S. Etheridge.

Figure 5.27. A. Volume scattering functions computed for particles with refractive index 1.05 + i 0.001, a Junge slope of 4 with increasing proportions of *P. micans* cells from 0% to 90% of total particle volume. The total particle volume was held constant, only the proportions change. Inset shows the first 2 degrees of resolution. B. The modeled values for beam attenuation coefficient versus the theoretical values for the two instruments as in Figures 14 to 16. As the proportion of *P. micans* increases, beam attenuation coefficients decrease, because phytoplankton are less efficient attenuaters than other weakly absorbing particles.

Figure 5.28. A. Volume scattering functions computed for particles with refractive index 1.05 + i 0.001, a Junge slope of 4 with increasing proportions of *Aureococcus anophagefferens* cells from 0% to 90% of total particle volume. The total particle volume has been held constant, only the proportion of *A. anophagefferens* cells relative to background particles changes. Inset shows the first 2 degrees of resolution. B. The modeled values for beam attenuation coefficient versus the theoretical values for the two instruments as in Figure 5.27. As the proportion of *A.. anophagefferens* increases, beam attenuation coefficient increases as the small *A. anophagefferens* cells are more efficient attenuaters than the larger background particles (which might consist of larger cells, aggregates, detrital matter, suspended sediments).

Figure 5.29. Time series of IOP observations during a brown tide bloom, Long Island, NY (Etheridge and Roesler, 2004): beam attenuation, absorption and chlorophyll from West Neck Bay (A) and Quantuck Bay (B), and slope of the particle beam attenuation coefficient (γ) for both sites (C). The phytoplankton community varied in both particle size and pigment composition at WNB although the bulk concentration remained stable. In contrast, a bloom of *Aureococcus anophagefferens* developed at QB as indicated by the increase in the IOP magnitudes and chlorophyll concentration. The indicator of size distribution remained invariant and indicative of small particles, consistent with the *A. anophagefferens* cell size (< 3 μm). These results were verified by microscopy and size fractionated HPLC pigment analyses.

Figure 5.30. Real time hourly observations of temperature, IOPs, and derived optical properties for the period August 2002 to January 2003 from the Eastern Maine Coastal Current, Gulf of Maine (Roesler and Barnard, 2003). A. Temperature at 0 m, 20 m, and 50 m, B. component absorption (440 nm, derived from total measured absorption, see text for details), C. particle backscattering ratio (660 nm), D. spectral slope of particle attenuation, γ, and E and F. spectral shape of two phytoplankton absorption components, the temporal pattern for each shown in part B. See text for details.